

# 1 Seamless mapping of long-term (2010-2020) daily global XCO<sub>2</sub> and 2 XCH<sub>4</sub> from GOSAT, OCO-2, and CAMS-EGG4 with a 3 spatiotemporally self-supervised fusion method

4 Yuan Wang<sup>1,2</sup>, Qiangqiang Yuan<sup>1</sup>, Tongwen Li<sup>3</sup>, Yuanjian Yang<sup>2</sup>, Siqin Zhou<sup>1</sup>, Liangpei Zhang<sup>4</sup>

5 <sup>1</sup>School of Geodesy and Geomatics, Wuhan University, Wuhan, Hubei, 430079, China.

6 <sup>2</sup>School of Atmospheric Physics, Nanjing University of Information Science & Technology, Nanjing, Jiangsu, 210044,  
7 China.

8 <sup>3</sup>School of Geospatial Engineering and Science, Sun Yat-sen University, Guangzhou, Guangdong, 519082, China.

9 <sup>4</sup>The State Key Laboratory of Information Engineering in Surveying, Mapping and Remote Sensing, Wuhan University,  
10 Wuhan, Hubei, 430079, China.

11 *Correspondence to:* Qiangqiang Yuan ([qyuan@sgg.whu.edu.cn](mailto:qyuan@sgg.whu.edu.cn))

12 **Abstract.** Precise and continuous monitoring on long-term carbon dioxide (CO<sub>2</sub>) and methane (CH<sub>4</sub>) over the globe is of great  
13 importance, which can help study global warming and achieve the goal of carbon neutrality. Nevertheless, the available  
14 observations of CO<sub>2</sub> and CH<sub>4</sub> from satellites are generally sparse, and current fusion methods to reconstruct their long-term  
15 values on a global scale are few. To address this problem, we propose a novel spatiotemporally self-supervised fusion method  
16 to establish long-term daily seamless XCO<sub>2</sub> and XCH<sub>4</sub> products from 2010 to 2020 over the globe at grids of 0.25°. A total of  
17 three datasets are applied in our study, including GOSAT, OCO-2, and CAMS-EGG4. Attributed to the significant sparsity of  
18 data from GOSAT and OCO-2, the spatiotemporal Discrete Cosine Transform is considered for our fusion task. Validation  
19 results show that the proposed method achieves a satisfactory accuracy, with the Standard-Deviation of Bias ( $\sigma$ ) of ~ 1.18 ppm  
20 for XCO<sub>2</sub> and 11.3 ppb for XCH<sub>4</sub> against TCCON measurements from 2010 to 2020. Meanwhile, the Determination-  
21 Coefficient ( $R^2$ ) of XCO<sub>2</sub> and XCH<sub>4</sub> reach 0.91/0.95 (2010-2014/2015-2020) and 0.9 (2010-2020) after fusion, respectively.  
22 Overall, the performance of fused results distinctly exceeds that of CAMS-EGG4, which is also superior or close to those of  
23 GOSAT and OCO-2. Especially, our fusion method can effectively correct the large biases in CAMS-EGG4 due to the issues  
24 from assimilation data, such as the unadjusted anthropogenic emission inventories for COVID-19 lockdowns in 2020.  
25 Moreover, the fused results present coincident spatial patterns with GOSAT and OCO-2, which accurately display the long-  
26 term and seasonal changes of globally distributed XCO<sub>2</sub> and XCH<sub>4</sub>. The daily global seamless gridded (0.25°) XCO<sub>2</sub> and  
27 XCH<sub>4</sub> from 2010 to 2020 can be freely accessed at <http://doi.org/10.5281/zenodo.7388893> (Wang et al., 2022b).

## 28 **1 Introduction**

29 As the most abundant greenhouse gases (GHGs) due to human activities, atmospheric carbon dioxide (CO<sub>2</sub>) and methane  
30 (CH<sub>4</sub>) play significant roles in climate change and directly contribute to global warming (Meinshausen et al., 2009; Montzka  
31 et al., 2011; Solomon et al., 2010; Yoro and Daramola, 2020; Shine et al., 2005). For decades, the rising anthropogenic surface  
32 emissions of CO<sub>2</sub> and CH<sub>4</sub> result in their long-term rapid uptrends (Choulga et al., 2021; Moran et al., 2022; Lin et al., 2021;  
33 Petrescu et al., 2021), which have greatly affected the carbon cycle (Battin et al., 2009; Sjögersten et al., 2014) and ecosystem  
34 balance (Liu and Greaver, 2009; Hotchkiss et al., 2015). According to measurements from the Global Greenhouse Gas  
35 Reference Network (<https://gml.noaa.gov/ccgg/>), annual surface CO<sub>2</sub> and CH<sub>4</sub> mole fractions break 412 parts per million (ppm)  
36 and 1878 parts per billion (ppb) in 2020, with growths of ~ 68 ppm and 222 ppb since 1985, respectively. To mitigate global  
37 warming, the Paris Agreement (<https://unfccc.int/process-and-meetings/the-paris-agreement/>) has indicated that the increment  
38 of temperature should not exceed 2 °C (preferably to 1.5 °C) by comparison with the pre-industrial level. This requires all  
39 efforts from the whole society to reach the global peaking of GHGs surface emissions as early as possible, especially for CO<sub>2</sub>  
40 and CH<sub>4</sub>, which eventually create a carbon-neutral world by mid-century. Therefore, it is an urgent need to precisely and  
41 continuously monitor atmospheric CO<sub>2</sub> and CH<sub>4</sub> on a global scale.

42 To date, remote sensing observations have been extensively adopted in plenty of domains (He et al., 2022c, 2023; Wang et al.,  
43 2021, 2022c; Xiao et al., 2022, 2023; Zhou et al., 2022), which also emerged as regular techniques to acquire globe-scale  
44 atmospheric CO<sub>2</sub> and CH<sub>4</sub> spatial patterns (He et al., 2022a; Buchwitz et al., 2015; Bergamaschi et al., 2013). For instance, the  
45 EnviSat can provide global column-mean dry-air mole fraction of CO<sub>2</sub> (XCO<sub>2</sub>) and CH<sub>4</sub> (XCH<sub>4</sub>) at a coarse resolution of  
46 30×60 km<sup>2</sup>, with the payload of the Scanning Imaging Absorption Spectrometer for Atmospheric Cartography (Burrows et al.,  
47 1995; Beirle et al., 2018). The Thermal and Near-Infrared Sensor for carbon Observations - Fourier Transform Spectrometer  
48 onboard the Greenhouse Gases Observing Satellite (GOSAT) (Hamazaki et al., 2005; Velazco et al., 2019) can produce ~ 10-  
49 km XCO<sub>2</sub> and XCH<sub>4</sub> over the globe based on three spectral bands. The Orbiting Carbon Observatory 2/3 (OCO-2/3) (Crisp et  
50 al., 2017; Doughty et al., 2022) carries three-channel grating spectrometers to generate globally covered XCO<sub>2</sub> at a much finer  
51 spatial resolution of 1.29×2.25 km<sup>2</sup>. The Carbon Dioxide Spectrometer named CarbonSpec onboard the TanSat (Liu et al.,  
52 2018) of China launched in 2016, which can accurately map high-resolution (~ 2 km) global XCO<sub>2</sub> spatial distribution.

53 As for long-term observations of XCO<sub>2</sub> and XCH<sub>4</sub>, the operational products from GOSAT and OCO-2 are widely applied in  
54 carbon-related applications, such as the computation of carbon fluxes (Fraser et al., 2013; Wang et al., 2019), inferring carbon  
55 sources and sinks (Deng et al., 2014; Houweling et al., 2015), quantifying CO<sub>2</sub> and CH<sub>4</sub> emissions (Turner et al., 2015;  
56 Hakkarainen et al., 2016), and estimation of terrestrial net ecosystem exchange (Jiang et al., 2022). Nevertheless, large-scale  
57 missing data consists in the XCO<sub>2</sub> and XCH<sub>4</sub> products from GOSAT and OCO-2, which is attributed to the narrow swath of  
58 their observations (Crisp et al., 2017) and contamination of cloud and aerosol (Taylor et al., 2016). Seamless information of

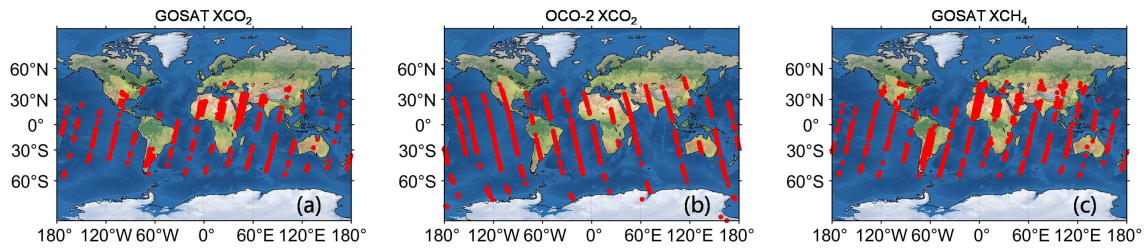
59 XCO<sub>2</sub> and XCH<sub>4</sub> can help better understand the driving factors of long-term variations for CO<sub>2</sub> and CH<sub>4</sub> due to surface  
60 emissions and atmospheric transport (Kenea et al., 2023; Liu et al., 2020). In addition, full-coverage XCO<sub>2</sub> and XCH<sub>4</sub> products  
61 are more useful to analyze carbon source-sink dynamics (Reithmaier et al., 2021; Crosswell et al., 2017) and impacts on climate  
62 changes caused by the elevated CO<sub>2</sub> and CH<sub>4</sub> (Chen et al., 2021; Le Quéré et al., 2019). Hence, it is significant and essential  
63 to assure the spatiotemporal continuity of XCO<sub>2</sub> and XCH<sub>4</sub> products from GOSAT and OCO-2, which is conducive to achieving  
64 the goal of carbon neutrality.

65 A lot of efforts have been made to generate seamless XCO<sub>2</sub> and XCH<sub>4</sub> products for GOSAT and OCO-2. Initially, interpolation-  
66 based methods are widely utilized, such as the fixed rank kriging interpolation (Katzfuss and Cressie, 2011), semantic kriging  
67 interpolation (Bhattacharjee et al., 2014), and space-time kriging interpolation (He et al., 2020; Li et al., 2022). However, the  
68 interpolated results are usually performed at coarse spatial resolutions (e.g., 1°) and tend to show high uncertainties and over-  
69 smoothed distribution due to the extreme sparsity of original data. At present, data fusion techniques (He et al., 2022a, b; Zhang  
70 et al., 2022; Zhang and Liu, 2023; Siabi et al., 2019) have emerged as new methods to acquire full-coverage products for  
71 GOSAT and OCO-2 at a high spatial resolution, which absorb advantages from multisource data. Generally, these methods  
72 exploited machine learning algorithms to train an end-to-end fusion function with multiple seamless data (e.g., model and  
73 reanalysis) as inputs. For example, Siabi et al. (2019) employed multi-layer perceptron and eight environmental variables (e.g.,  
74 net primary productivity and leaf area index) to map full-coverage XCO<sub>2</sub> in Iran; He et al. (2022b) established seamless results  
75 over China using the OCO-2 XCO<sub>2</sub> product, CarbonTracker model data, and auxiliary co-variates based on the light gradient  
76 boosting machine; Zhang et al. (2022) proposed a geographically weighted neural network to produce full-coverage XCO<sub>2</sub>  
77 product across China by fusing the datasets from OCO-2, CAMS-EGG4 (reanalysis), and ERA5; and Zhang and Liu (2023)  
78 adopted multiple datasets, e.g., EnviSat, GOSAT, OCO-2, CarbonTracker, and ERA5, and obtained long-term seamless XCO<sub>2</sub>  
79 product in China through a finely devised neural network.

80 These data fusion approaches provided high-quality results with seamless distribution and greatly enhance the data availability  
81 for GOSAT and OCO-2. Nevertheless, the application areas of current fused products merely target at local or national scales,  
82 which are insufficient for globe-scale researches. Meanwhile, existing data fusion frameworks are regarded as end-to-end  
83 functions, which lack consideration for spatiotemporal self-correlation of original data (e.g., OCO-2). They normally require  
84 massive auxiliary co-variates (e.g., ERA5) as inputs and consume a large time in training procedures. Moreover, only XCO<sub>2</sub>  
85 products are taken into account while the data fusion studies for XCH<sub>4</sub> products are scarce. In conclusion, it is valuable and  
86 imperative to generate long-term globally distributed seamless XCO<sub>2</sub> and XCH<sub>4</sub> products for GOSAT and OCO-2 with an  
87 efficient data fusion method, which considers the knowledge of their spatiotemporal self-correlation.

88 The present study focuses on generating long-term daily global seamless XCO<sub>2</sub> and XCH<sub>4</sub> products from 2010 to 2020 at the  
89 grids of 0.25° via a spatiotemporally self-supervised fusion method. A total of three datasets are utilized in our study without

90 any auxiliary co-variates, including GOSAT, OCO-2, and CAMS-EGG4. CAMS-EGG4 can provide long-term gridded full-  
 91 coverage XCO<sub>2</sub> and XCH<sub>4</sub> datasets over the globe, which is suitable for our fusion task. Since the data from GOSAT and OCO-  
 92 2 is significantly sparse in space-time domain (see Fig. 1), the fusion procedures are difficult to be performed. By contrast,  
 93 frequency domain contains comprehensive information due to its more concentrated signal distribution. Discrete Cosine  
 94 Transform (DCT) (Rao and Yip, 2014) is an efficient algorithm to convert signal into frequency domain. In this study, a novel  
 95 self-supervised fusion method based on spatiotemporal DCT (S-STDCT) is developed for the fusion task. Details of the S-  
 96 STDCT fusion method are presented in Section 3. Validation results show that the S-STDCT fusion method achieves a  
 97 satisfactory performance. Generally, the accuracy of fused results largely exceeds that of CAMS-EGG4, which is also better  
 98 than or close to those of GSOAT and OCO-2.



99  
 100 **Figure 1.** An example of daily spatial footprints for (a) GOSAT XCO<sub>2</sub>, (b) OCO-2 XCO<sub>2</sub>, and (c) GOSAT XCH<sub>4</sub>. Red points signify the  
 101 available data. Background maps are naturally shaded reliefs over the globe.

102 This paper arranges the remaining sections as follows. Section 2 describes the data records employed in our study, including  
 103 the XCO<sub>2</sub> and XCH<sub>4</sub> from in-situ stations, GOSAT, and CAMS-EGG4 and XCO<sub>2</sub> from OCO-2. Section 3 provides the  
 104 specification of the developed S-STDCT fusion method. Section 4 presents the experiment results, which consist of elaborative  
 105 validations against in-situ measurements and assessments of spatial distribution on multi-temporal scales. At last, conclusions  
 106 and future works are summarized in section 5.

## 107 2 Data description

### 108 2.1 GOSAT XCO<sub>2</sub> and XCH<sub>4</sub> products

109 A famous XCO<sub>2</sub> retrieval algorithm devised for GOSAT (Taylor et al., 2022), i.e., the Atmospheric CO<sub>2</sub> Observations from  
 110 Space (ACOS), employs three infrared spectral bands at ~ 0.76, 1.6, and 2.0 μm, which are denoted as Oxygen-A, CO<sub>2</sub> weak,  
 111 and CO<sub>2</sub> strong, respectively. Regarding XCH<sub>4</sub>, the latest retrieval algorithm for GOSAT from the University of Leicester is  
 112 recently updated, which considers the ratio of XCH<sub>4</sub>:XCO<sub>2</sub> as a proxy (Parker et al., 2020). It is based on the theory that the  
 113 impacts from atmospheric scattering and sensor are mostly similar for XCH<sub>4</sub> and XCO<sub>2</sub> in a shared absorption band at ~ 1.6  
 114 μm. The GOSAT XCO<sub>2</sub> and XCH<sub>4</sub> products are both performed at spatial resolutions of 10.5 km (diameter) over the globe  
 115 with revisit times of 3 days. In our study, the scientific data records of “XCO2” in ACOS\_L2\_Lite\_FP (level 2, bias-corrected,  
 116 V9r) and “XCH4” in UoL-GHG-L2-CH4-GOSAT-OCPR (level 2, V9) are adopted. Furthermore, the quality assurance (QA)



117 records of “XCO<sub>2</sub> Quality Flag” and “XCH<sub>4</sub> Quality Flag” are exploited to filter bad data. Relevant information of XCO<sub>2</sub> and  
 118 XCH<sub>4</sub> products from GOSAT is shown in Table 1.

119 **Table 1.** Detailed information of the datasets considered in this study.

Source	Scientific data record	Version	Spatial resolution	Temporal resolution	Period
GOSAT	XCO <sub>2</sub> XCO <sub>2</sub> Quality Flag	V9r	10.5 km (diameter)	Daily (~ 13:00 local time)	2010-2014
	XCH <sub>4</sub> XCH <sub>4</sub> Quality Flag	V9			2010-2020
OCO-2	XCO <sub>2</sub> XCO <sub>2</sub> Quality Flag	V10r	1.29×2.25 km <sup>2</sup>	Daily (~ 13:36 local time)	2015-2017
	XCO <sub>2</sub> XCO <sub>2</sub> Quality Flag	V11r			2018-2020
CAMS-EGG4	CO <sub>2</sub> column-mean molar fraction	-	0.75°	3 hours	2010-2020
	CH <sub>4</sub> column-mean molar fraction				

## 120 2.2 OCO-2 XCO<sub>2</sub> product

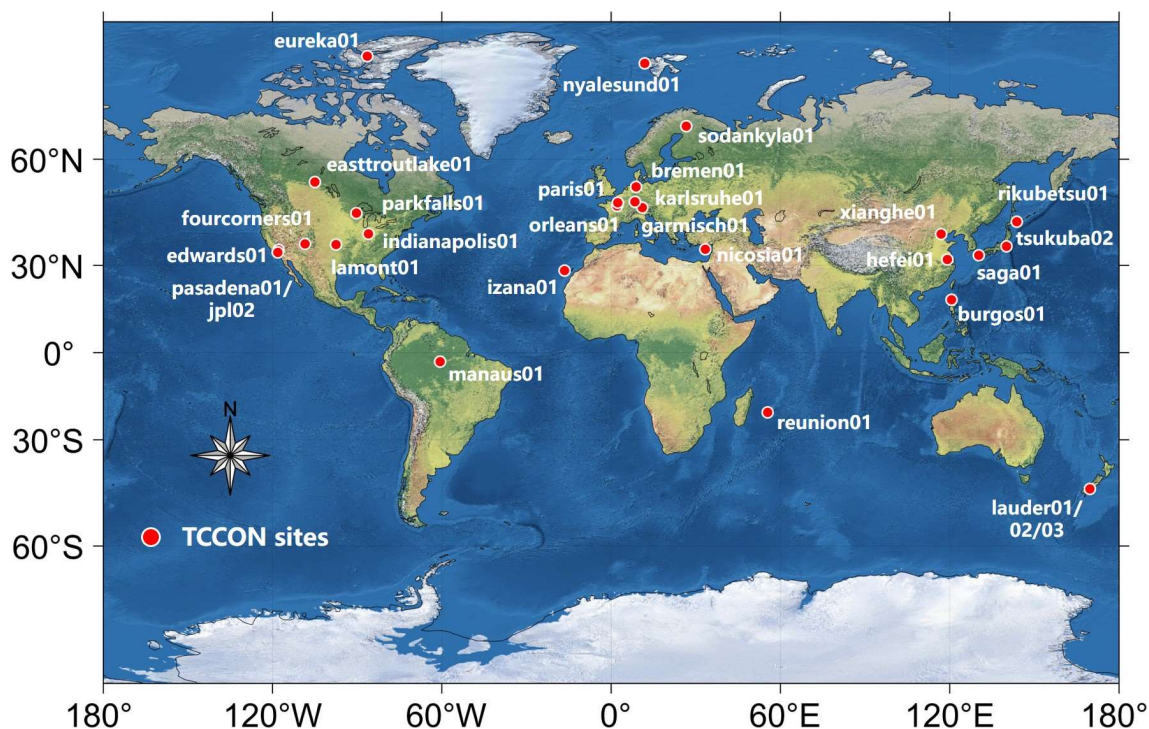
121 Apart from GOSAT, the ACOS XCO<sub>2</sub> retrieval algorithm is also applied to OCO-2 observations (Kiel et al., 2019), which  
 122 utilizes the same bands of the Oxygen-A, CO<sub>2</sub> weak, and CO<sub>2</sub> strong. OCO-2 provides a global XCO<sub>2</sub> product at a high spatial  
 123 resolution of 1.29×2.25 km<sup>2</sup> with a revisit time of 16 days. After 2015, the XCO<sub>2</sub> product from OCO-2 is used for fusion  
 124 instead of GOSAT due to its more observation counts and better accuracy. In this study, the scientific data record of “XCO<sub>2</sub>”  
 125 in OCO2\_L2\_Lite\_FP (level 2, bias-corrected) is applied in the fusion with CAMS-EGG4 using the developed method.  
 126 Moreover, the QA record of “XCO<sub>2</sub> Quality Flag” is adopted to filter bad data. Since the OCO-2 XCO<sub>2</sub> product of the latest  
 127 version (V11r) is still on processing, both data of V10r and V11r are considered in our study. Related information of XCO<sub>2</sub>  
 128 product from OCO-2 is given in Table 1.

## 129 2.3 CAMS-EGG4 GHGs reanalysis datasets

130 CAMS-EGG4 is recent globally distributed operational GHGs reanalysis datasets supported by the European Centre for  
 131 Medium-range Weather Forecasts (Agusti-Panareda et al., 2022). It assimilates the forecasts from the Integrated Forecasting  
 132 System with multiple satellite products, which include Envisat, GOSAT, and Metop-A/B (August et al., 2012), via physical  
 133 and chemistry principles. The CAMS-EGG4 can generate long-term gridded seamless XCO<sub>2</sub> and XCH<sub>4</sub> datasets and related  
 134 fields at spatial and temporal resolutions of 0.75° and 3 hours, respectively. Unfortunately, there are a few limitations in CAMS-  
 135 EGG4, such as the uncorrected anthropogenic emissions for CO<sub>2</sub> and CH<sub>4</sub> during COVID-19 lockdowns, which are  
 136 scheduled to be fixed by the official team in the future (Agusti-Panareda et al., 2022). It is worth noting that the XCO<sub>2</sub> and  
 137 XCH<sub>4</sub> products from GOSAT and OCO-2 employed in this paper are not assimilated in CAMS-EGG4. In our study, the  
 138 scientific data records of “CO<sub>2</sub> column-mean molar fraction” and “CH<sub>4</sub> column-mean molar fraction” are exploited for the  
 139 fusion with GOSAT and OCO-2 through the developed method. Details of CAMS-EGG4 datasets are provided in Table 1.

## 140 2.4 TCCON measurements

141 In our study, the XCO<sub>2</sub> and XCH<sub>4</sub> measurements provided by an international in-situ network, which is named after TCCON  
142 (Wunch et al., 2011) (<https://tccn.org/>), are utilized to validate the fused results. The in-situ measurements of TCCON  
143 are extensively used in the validation for XCO<sub>2</sub> and XCH<sub>4</sub> products from GOSAT, OCO-2, and CAMS-EGG4 (Hong et al.,  
144 2022; Yoshida et al., 2013; Wunch et al., 2017; Wu et al., 2018; Agusti-Panareda et al., 2022). Figure 2 depicts the spatial  
145 locations of TCCON stations, with the marks of white-edged red circles. The measurements of version GGG2020 (Laughner  
146 et al., 2022) from 29 stations around the world are adopted. Specific information of the stations is listed in Table 2.



147  
148 **Figure 2.** Spatial locations of in-situ stations from TCCON used in the present study. The background map is a naturally shaded relief over  
149 the globe.

## 150 3 Methodology

### 151 3.1 Data pre-processing

152 Data pre-processing is an important procedure to ensure the rationality and reliability of fused results. In this study, the values  
153 of “QA=0” in XCO<sub>2</sub> and XCH<sub>4</sub> from GOSAT and OCO-2 are discarded, which filters the bad data. Besides, the CAMS-EGG4  
154 XCO<sub>2</sub> and XCH<sub>4</sub> at a temporal resolution of 3 hours are averaged in a single day to produce daily datasets. Finally, the spatial  
155 resolutions of XCO<sub>2</sub> and XCH<sub>4</sub> from GOSAT, OCO-2, and CAMS-EGG4 ought to be adjusted to the same value. A globally  
156 covered grid of 721×1441 (0.25°) is employed in our study. The XCO<sub>2</sub> and XCH<sub>4</sub> from GOSAT, OCO-2, and CAMS-EGG4  
157 are re-gridded to 0.25° using the area-weighted aggregation (Wang et al., 2021) and Inverse Distance Weighted (Mueller et al.,  
158 2004) interpolation, respectively.

159 **Table 2.** Detailed information of TCCON in-situ stations adopted in our study. No.: number.

No.	Site name	Latitude	Longitude	Location	Start date	End date
1	bremen01	53.10	8.85	Europe	2010-01-01	2020-12-31
2	burgos01	18.53	120.65	Asia	2017-03-03	2020-04-30
3	easttroutlake01	54.36	-104.99	North America	2016-10-03	2020-12-31
4	edwards01	34.96	-117.88	North America	2013-07-20	2020-12-31
5	eureka01	80.05	-86.42	North America	2010-07-24	2020-07-07
6	fourcorners01	36.80	-108.48	North America	2013-03-16	2013-10-03
7	garmisch01	47.48	11.06	Europe	2010-01-01	2020-12-31
8	hefei01	31.90	119.17	Asia	2016-01-08	2020-12-31
9	indianapolis01	39.86	-86.00	North America	2012-08-23	2012-12-01
10	izana01	28.31	-16.50	Atlantic Ocean	2014-01-02	2020-12-31
11	jpl02	34.20	-118.18	North America	2011-05-19	2018-05-14
12	karlsruhe01	49.10	8.44	Europe	2014-01-15	2020-12-31
13	lauder01	36.60	-97.49	Oceania	2010-01-01	2010-02-19
14	lauder02	-45.04	169.68	Oceania	2013-01-02	2018-09-30
15	lauder03	-45.04	169.68	Oceania	2018-10-02	2020-12-31
16	lamont01	-45.04	169.68	North America	2010-01-01	2020-12-31
17	manaus01	-3.21	-60.60	South America	2014-09-30	2015-07-27
18	nicosia01	35.14	33.38	Asia	2019-09-03	2020-12-31
19	nyalesund01	78.92	11.92	Arctic Ocean	2010-01-01	2020-12-31
20	orleans01	47.96	2.11	Europe	2010-01-01	2020-12-31
21	paris01	48.85	2.36	Europe	2014-09-23	2020-12-31
22	parkfalls01	45.94	-90.27	North America	2010-01-01	2020-12-31
23	pasadena01	34.14	-118.13	North America	2012-09-20	2020-12-31
24	reunion01	-20.90	55.48	Indian Ocean	2015-03-01	2020-07-18
25	rikubetsu01	43.46	143.77	Asia	2014-06-24	2020-12-31
26	saga01	33.24	130.29	Asia	2011-07-28	2020-12-31
27	sodankyla01	67.37	26.63	Europe	2018-03-05	2020-12-31
28	tsukuba02	36.05	140.12	Asia	2014-03-28	2020-12-31
29	xianghe01	39.80	116.96	Asia	2018-06-14	2020-12-31

160 **3.2 Spatiotemporally self-supervised fusion method**

161 Since the sparsity of data from GOSAT and OCO-2 is significant in space-time domain (see Fig. 1), it is difficult to perform  
162 fusion procedures for them. In contrast, frequency domain is more suitable because of its concentrated signal distribution. DCT  
163 is an efficient algorithm to transform signal into frequency domain (Rao and Yip, 2014), which has been widely applied in  
164 image compression (Cintra and Bayer, 2011), geophysical data filtering (El-Mahallawy and Hashim, 2013), and remote sensing  
165 data reconstruction (Wang et al., 2012, 2022a; Fredj et al., 2016; Pham et al., 2019). In our study, a novel self-supervised fusion  
166 method based on spatiotemporal DCT, i.e., S-STDCT, is developed for the fusion task, which fully adopts the spatiotemporal  
167 knowledge of self-correlation in GOSAT and OCO-2 products.

168 **3.2.1 Spatiotemporal DCT**

169 A total of eight types of DCT are proposed, among which the second type (type-II) is commonly utilized due to its simple  
170 calculation and broad application range (Rao and Yip, 2014). Hence, the type-II DCT is considered in this study. The  
171 spatiotemporal DCT is a 3-dimensional form (hereafter *STDCT*), which can be expressed as Eq. (1):

$$172 \quad X(u, v, w) = c(u)c(v)c(w) \sum_{i=0}^{M-1} \sum_{j=0}^{N-1} \sum_{t=0}^{P-1} x(i, j, t) \cos \left[ \frac{(i+0.5)\pi}{M} u \right] \cos \left[ \frac{(j+0.5)\pi}{N} v \right] \cos \left[ \frac{(t+0.5)\pi}{P} w \right], \quad (1)$$

$$173 \quad \text{where } c(u) = \begin{cases} \sqrt{\frac{1}{M}}, u = 0 \\ \sqrt{\frac{2}{M}}, u \neq 0 \end{cases}, \quad c(v) = \begin{cases} \sqrt{\frac{1}{N}}, v = 0 \\ \sqrt{\frac{2}{N}}, v \neq 0 \end{cases}, \quad c(w) = \begin{cases} \sqrt{\frac{1}{P}}, w = 0 \\ \sqrt{\frac{2}{P}}, w \neq 0 \end{cases};$$

;  $x$  indicates the original 3-dimensional tensor;  $M, N,$

174 and  $P$  stand for the counts of rows (latitude), columns (longitude), and temporal sequences (days), which equal 721 (0.25°,  
 175 global grids), 1441 (0.25°, global grids), and days of a year (365 or 366), respectively;  $i, j,$  and  $t$  represent the row, column,  
 176 and temporal sequence, respectively ( $i \in [0, M-1], j \in [0, N-1],$  and  $t \in [0, P-1]$ );  $X$  signifies the transformed 3-dimensional  
 177 tensor;  $u, v,$  and  $w$  denote the transformed coordinates in frequency domain, which share the same ranges with  $i, j,$  and  $t$  (e.g.,  
 178  $u \in [0, M-1]$ ), respectively. The inverse transformation of *STDCT* (hereafter *ISTDCT*) is provided in Eq. (2):

$$179 \quad x(i, j, t) = c(u)c(v)c(w) \sum_{u=0}^{M-1} \sum_{v=0}^{N-1} \sum_{w=0}^{P-1} X(u, v, w) \cos \left[ \frac{(i+0.5)\pi}{M} u \right] \cos \left[ \frac{(j+0.5)\pi}{N} v \right] \cos \left[ \frac{(t+0.5)\pi}{P} w \right], \quad (2)$$

### 180 3.2.2 Self-supervised fusion scheme with spatiotemporal knowledge

181 It has been documented that the  $XCO_2$  and  $XCH_4$  products derived from remote sensing satellites generally present better  
 182 accuracy compared to reanalysis datasets (Agusti-Panareda et al., 2022; He et al., 2022a; Parker et al., 2020). Therefore, the  
 183 brand new  $XCO_2$  and  $XCH_4$  products from GOSAT and OCO-2 are regarded as the criteria (or ground truths), which will be  
 184 fused with CAMS-EGG4 datasets. At first, a spatially and temporally varying function relationship (see Eq. (3)) is  
 185 hypothesized between GOSAT/OCO-2 and CAMS-EGG4  $XCO_2/XCH_4$  values.

$$186 \quad XG_s = f(XG_c, Row, Col, Time), \quad (3)$$

187 where  $XG_s$  denotes the  $XCO_2/XCH_4$  values from GOSAT/OCO-2;  $XG_c$  indicates the  $XCO_2/XCH_4$  values from CAMS-EGG4;  
 188  $Row, Col,$  and  $Time$  represent the row (or latitude), column (or longitude), and temporal sequence, respectively. To conveniently  
 189 solve this problem, Eq. (3) is simplified into the scalar product form of  $XG_c$  and a spatially and temporally varying tensor  
 190 (defined as  $\delta$ ), as shown in Eq. (4):

$$191 \quad XG_s = XG_c * \delta(Row, Col, Time), \quad (4)$$

192 Afterward, the factor (i.e.,  $\delta$ ) can be acquired using the  $XCO_2/XCH_4$  values at the grids where the GOSAT/OCO-2 and CAMS-  
 193 EGG4 data are both available. In our study, a self-supervised fusion scheme is introduced to solve Eq. (4) based on the  
 194 spatiotemporal knowledge of self-correlation in GOSAT and OCO-2 products. Due to the large sparsity of data from GOSAT  
 195 and OCO-2 in space-time domain, the *STDCT* is applied for the fusion task.

196 Inspired by previous studies adopting the *STDCT* (Garcia, 2010; Wang et al., 2012, 2022a; Fredj et al., 2016; Pham et al.,  
 197 2019), the S-STDCT fusion method searches for the spatially and temporally varying tensor, i.e.,  $\hat{\delta}$ , that minimizes Eq. (5),  
 198 including a residual (left) and a smoothing (right) term.

$$199 \quad E(\delta) = \left\| \varphi^{\frac{1}{2}} * (\delta - \hat{\delta}) \right\|^2 + \varepsilon \|\nabla^2 \delta\|^2, \quad (5)$$

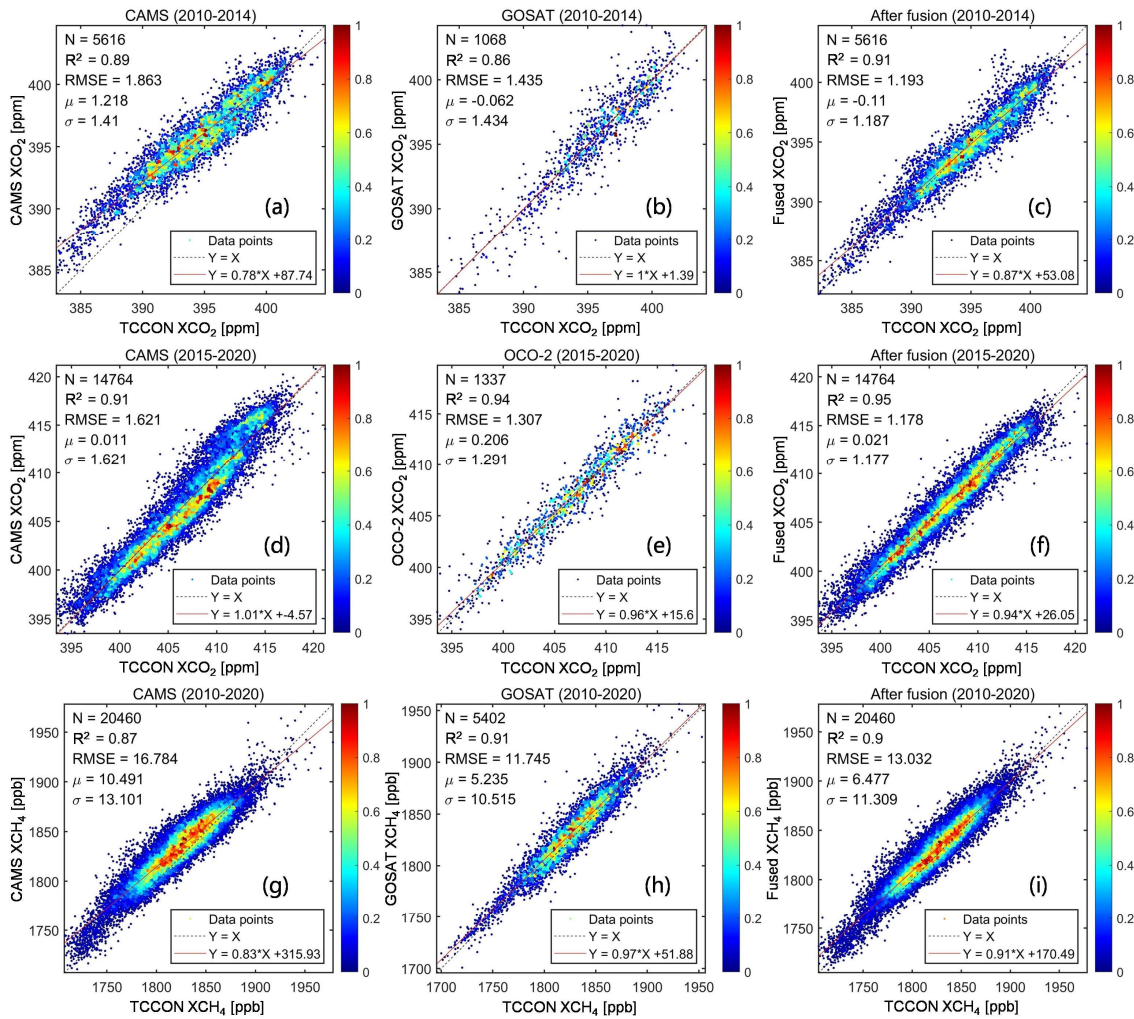
200 where  $\| \cdot \|$  signifies the Euclidean norm;  $\varphi$  represents the binary mask showing the data is whether available or not;  $\varepsilon$  and  
 201  $\nabla^2$  indicate a smoothing factor and the Laplace operator, respectively. This equation can be solved by iterations via Eq. (6):

$$202 \quad \hat{\delta} = \gamma \text{ISTDCT}(\rho * \text{STDCT}(\varphi * (\delta - \hat{\delta}) + \hat{\delta})) + (1 - \gamma)\hat{\delta}, \quad (6)$$

203 where  $\gamma$  is a relaxation factor to accelerate convergence;  $\rho$  indicates a 3-dimensional filter related to the smoothing term,  
 204 which is defined in Eq. (7):

$$205 \quad \rho(d_1, d_2, d_3) = \frac{1}{1 + \varepsilon \sum_{k=1}^3 2 \left[ 1 - \cos \left( \frac{d_k - 1}{n_k} \pi \right) \right]}, \quad (7)$$

206 Here,  $d_k$  represents the  $d^{\text{th}}$  value along the  $k^{\text{th}}$  dimension ( $k = 1, 2, \text{ and } 3$ );  $n_k$  denotes the size of  $\delta$  along the  $k^{\text{th}}$  dimension.  
 207 Namely,  $d_1$ ,  $d_2$ , and  $d_3$  stand for  $u$ ,  $v$ , and  $w$  (see Eq. (1)), respectively. In this study, the number of total iterations,  $\gamma$ , and  
 208  $\varepsilon$  are empirically configured to 100, 1.5, and a range from  $10^3$  to  $10^{-1}$  (spaced with 100 intervals), respectively. It is worth  
 209 noting that  $\hat{\delta}$  is initialized through the spatiotemporal nearest neighbor interpolation. More details about the solution steps  
 210 can be found in Garcia (2010).

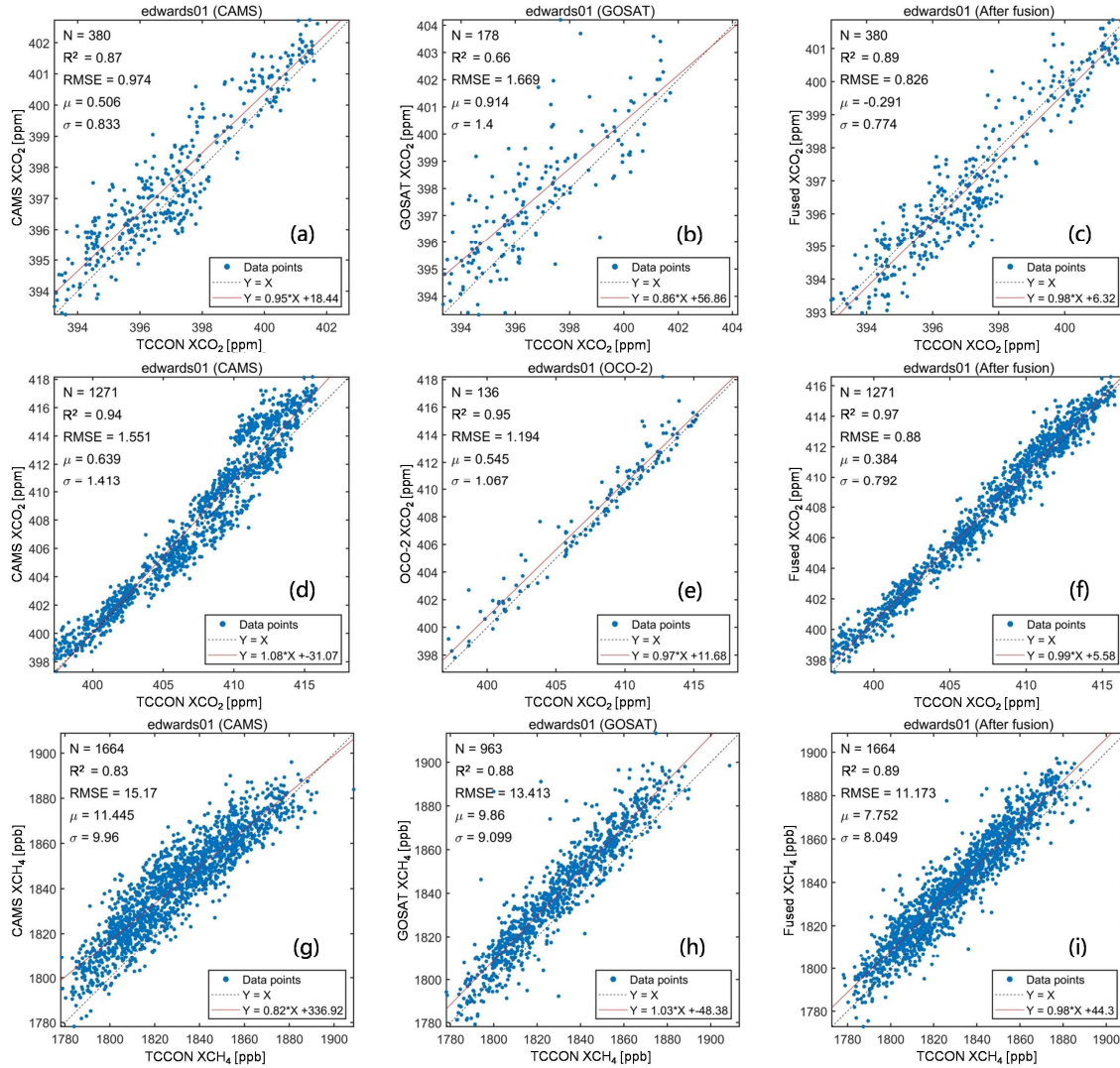


211  
 212 **Figure 3.** Density scatter-plots of the in-situ validation results for (a, d, and g) CAMS-EGG4, (b and h) GOSAT, (e) OCO-2, and (c, f, and  
 213 i) fused results. Black dotted and red full lines stand for the 1:1 and fitted lines, respectively. Color ramps show the normalized densities of  
 214 data points. X: TCCON data; Y: CAMS-EGG4/GOSAT/OCO-2/fused data. Unit: ppm/ppb to XCO<sub>2</sub>/XCH<sub>4</sub> for RMSE,  $\mu$ , and  $\sigma$ .



### 215 3.3 Evaluation schemes

216 In our study, the evaluation schemes include in-situ validations and assessments of spatial distribution. To be specific, the  
 217 GOSAT, OCO-2, CAMS-EGG4, and fused XCO<sub>2</sub> and XCH<sub>4</sub> are validated against TCCON measurements, which consists of  
 218 the comparisons for overall and individual in-situ stations. The spatial distribution of the GOSAT, OCO-2, CAMS-EGG4, and  
 219 fused XCO<sub>2</sub> and XCH<sub>4</sub> are assessed on multi-temporal scales, i.e., multi-year mean, seasonal, and annual. A total of four metrics  
 220 are exploited, covering the Determination-Coefficient (R<sup>2</sup>), Root-Mean-Square-Error (RMSE), Mean-Bias ( $\mu$ ), and Standard-  
 221 Deviation of Bias ( $\sigma$ ). The significance levels of  $p < 0.01$  are applied in the computations of all metrics.



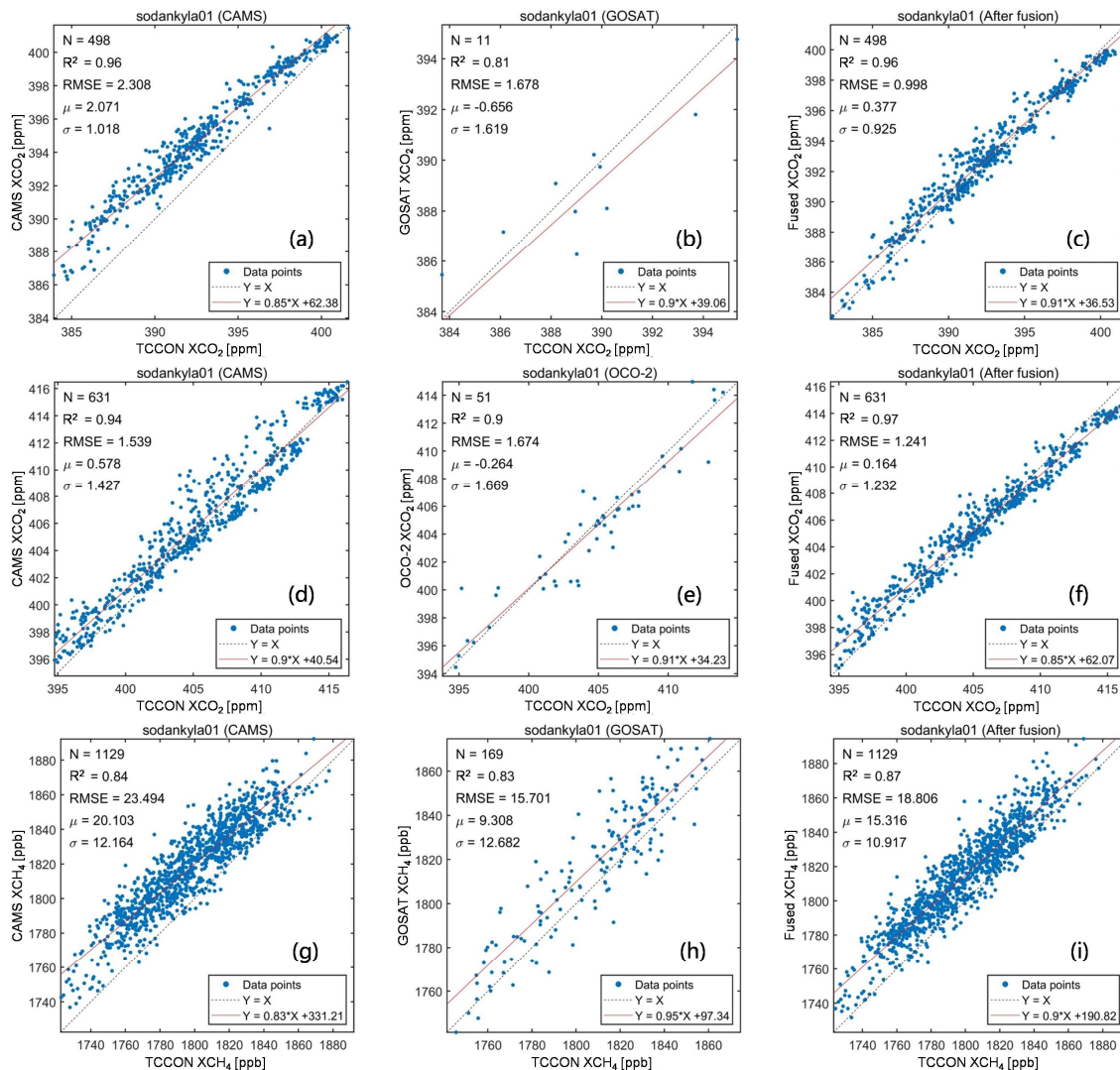
222  
 223 **Figure 4.** Scatter-plots of the in-situ validation results for (a, d, and g) CAMS-EGG4, (b and h) GOSAT, (e) OCO-2, and (c, f, and i) fused  
 224 results on edwards01. Black dotted and red full lines stand for the 1:1 and fitted lines, respectively. X: TCCON data; Y: CAMS-  
 225 EGG4/GOSAT/OCO-2/fused data. Unit: ppm/ppb to XCO<sub>2</sub>/XCH<sub>4</sub> for RMSE,  $\mu$ , and  $\sigma$ .

## 226 4 Experiment results and discussions

### 227 4.1 Overall in-situ validation

228 As displayed in Fig. 2, the XCO<sub>2</sub> and XCH<sub>4</sub> measurements from 29 TCCON in-situ stations are adopted for the validation,  
 229 which evenly distribute over the globe. In this study, TCCON measurements of  $\pm 1$  hour on the satellite overpass times ( $\sim$

230 13:00 and 13:36 local time, see Table 2) are co-matched with the CAMS-EGG4/GOSAT/OCO-2/fused data around each station  
 231 with a diameter of 2°. Figure 3 depicts the overall in-situ validation results for the CAMS-EGG4, GOSAT, OCO-2, and fused  
 232 results. The amounts of data points (N) are sufficient (e.g., 1337 for OCO-2 XCO<sub>2</sub> and 5402 for GOSAT XCH<sub>4</sub>) to support the  
 233 reliability of validation results.



234  
 235 **Figure 5.** Scatter-plots of the in-situ validation results for (a, d, and g) CAMS-EGG4, (b and h) GOSAT, (e) OCO-2, and (c, f, and i) fused  
 236 results on sodankyla01. Black dotted and red full lines stand for the 1:1 and fitted lines, respectively. X: TCCON data; Y: CAMS-  
 237 EGG4/GOSAT/OCO-2/fused data. Unit: ppm/ppb to XCO<sub>2</sub>/XCH<sub>4</sub> for RMSE,  $\mu$ , and  $\sigma$ .

238 As shown in Fig. 3, the XCO<sub>2</sub> from OCO-2 and XCH<sub>4</sub> from GOSAT perform better than those from CAMS-EGG4, with larger  
 239 R<sup>2</sup>, smaller RMSE, and smaller  $\sigma$ . After fusion, the XCO<sub>2</sub> (2015-2020) and XCH<sub>4</sub> (2010-2020) present a greatly superior  
 240 accuracy compared to CAMS-EGG4, of which the RMSE ( $\sigma$ ) improvements are 0.443 (0.444) ppm and 3.752 (1.792) ppb for  
 241 XCO<sub>2</sub> and XCH<sub>4</sub>, respectively. Meanwhile, the accuracy of the fused results is higher than and close to those of OCO-2 XCO<sub>2</sub>  
 242 and GOSAT XCH<sub>4</sub>, respectively. These suggest that the proposed fusion method achieves a satisfactory result. Furthermore,  
 243 the performance of XCO<sub>2</sub> from GOSAT is similar to that of CAMS-EGG4. However, the fused XCO<sub>2</sub> (2010-2014) shows  
 244 higher accuracy by comparison with both CAMS-EGG4 and GOSAT, indicating the spatiotemporally local fusion ability of S-  
 245 STDCT. In conclusion, our fusion method can successfully fuse the data from CAMS-EGG4 and satellites, which effectively



246 generates GOSAT-like and OCO-2-like values.

247 **Table 3.** Metrics of the individual in-situ validation results for CAMS-EGG4, GOSAT, and fused XCO<sub>2</sub>. The best and second metrics are  
 248 denoted with bold and underlined fonts. CAMS: CAMS-EGG4; AF: after fusion. Unit: ppm for RMSE and  $\sigma$ .

Site name	R <sup>2</sup>			RMSE			$\sigma$		
	CAMS	GOSAT	AF	CAMS	GOSAT	AF	CAMS	GOSAT	AF
bremen01	<u>0.91</u>	0.85	<b>0.92</b>	2.810	<u>1.732</u>	<b>1.533</b>	<u>1.376</u>	1.757	<b>1.189</b>
edwards01	<u>0.87</u>	0.66	<b>0.89</b>	<u>0.974</u>	1.669	<b>0.826</b>	<u>0.833</u>	1.400	<b>0.774</b>
fourcorners01	<u>0.88</u>	<b>0.91</b>	0.86	1.237	<u>0.867</u>	<b>0.844</b>	0.848	<b>0.590</b>	<u>0.801</u>
garmisch01	<u>0.91</u>	0.86	<b>0.93</b>	2.141	<u>1.575</u>	<b>1.070</b>	<u>1.275</u>	1.592	<b>1.067</b>
jpl02	<u>0.89</u>	0.86	<b>0.90</b>	1.535	<u>1.299</u>	<b>1.075</b>	<u>0.961</u>	1.299	<b>0.918</b>
saga01	0.90	<u>0.91</u>	<b>0.93</b>	<u>1.362</u>	1.494	<b>1.333</b>	1.313	<u>1.201</u>	<b>1.065</b>
lauder02	<u>0.83</u>	0.70	<b>0.87</b>	<b>0.584</b>	1.095	<u>0.606</u>	<b>0.585</b>	1.088	<u>0.600</u>
lamont01	<u>0.79</u>	<b>0.88</b>	<b>0.88</b>	1.928	<u>0.986</u>	<b>0.976</b>	1.327	<b>0.973</b>	<u>0.976</u>
orleans01	<u>0.89</u>	0.75	<b>0.91</b>	2.105	<u>1.666</u>	<b>0.964</b>	<u>1.144</u>	1.440	<b>0.964</b>
parkfalls01	<u>0.92</u>	0.86	<b>0.93</b>	2.088	<u>1.703</u>	<b>1.138</b>	<u>1.309</u>	1.697	<b>1.137</b>
pasadena01	0.70	<u>0.74</u>	<b>0.75</b>	<b>1.260</b>	<u>1.296</u>	1.642	<u>1.261</u>	1.287	<b>1.177</b>
sodankyla01	<b>0.96</b>	<u>0.81</u>	<b>0.96</b>	2.308	<u>1.678</u>	<b>0.998</b>	<u>1.018</u>	1.619	<b>0.925</b>
tsukuba02	<u>0.80</u>	<b>0.82</b>	0.78	<b>1.179</b>	1.651	<u>1.494</u>	<b>1.157</b>	1.263	<u>1.202</u>

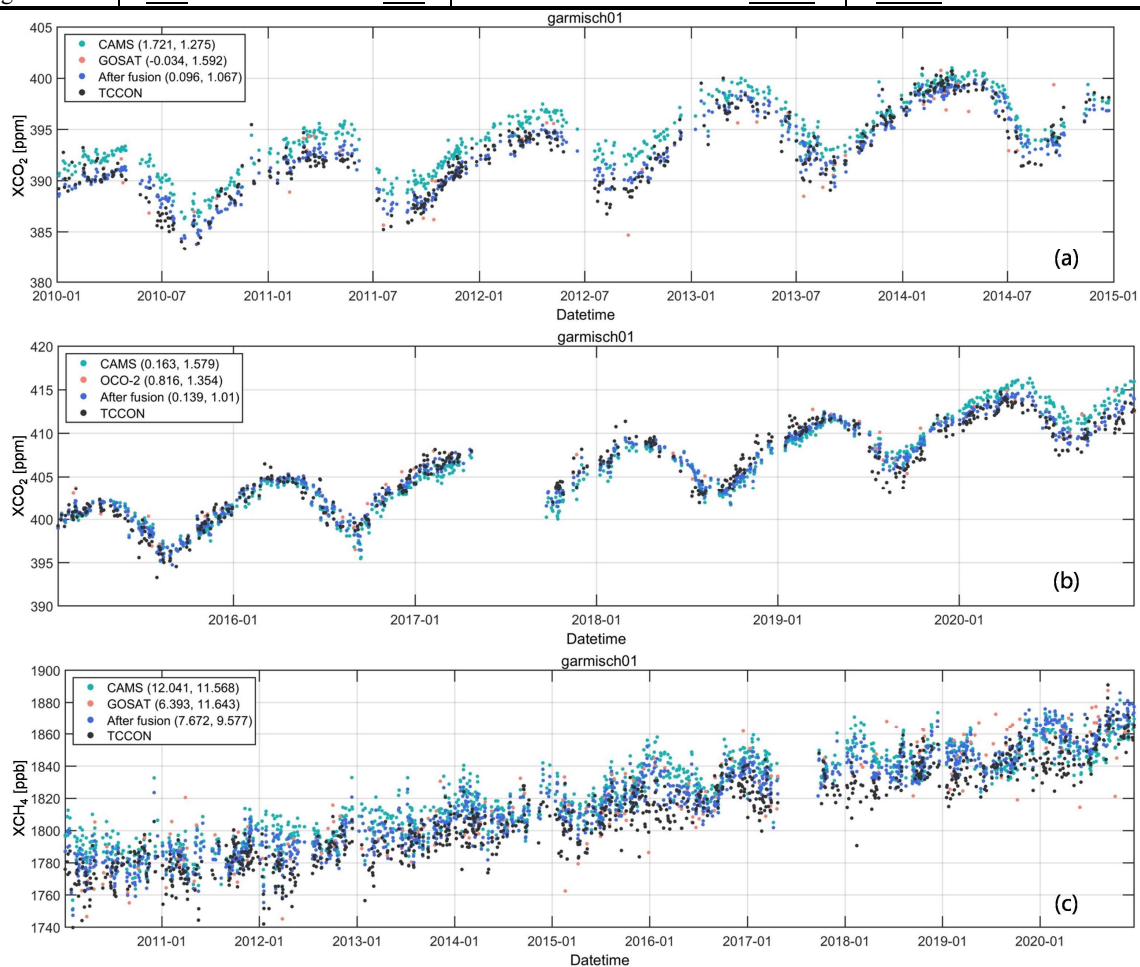
249 **Table 4.** Metrics of the individual in-situ validation results for CAMS-EGG4, OCO-2, and fused XCO<sub>2</sub>. The best and second metrics are  
 250 denoted with bold and underlined fonts. CAMS: CAMS-EGG4; AF: after fusion. Unit: ppm for RMSE and  $\sigma$ .

Site name	R <sup>2</sup>			RMSE			$\sigma$		
	CAMS	OCO-2	AF	CAMS	OCO-2	AF	CAMS	OCO-2	AF
bremen01	0.91	<b>0.99</b>	<u>0.93</u>	1.718	<b>1.126</b>	<u>1.476</u>	1.678	<b>1.066</b>	<u>1.459</u>
burgos01	0.91	<b>0.95</b>	<u>0.94</u>	1.324	<b>0.715</b>	<u>0.933</u>	1.144	<b>0.709</b>	<u>0.823</u>
edwards01	0.94	<u>0.95</u>	<b>0.97</b>	1.551	<u>1.194</u>	<b>0.880</b>	1.413	<u>1.067</u>	<b>0.792</b>
easttroutlake01	<u>0.92</u>	0.87	<b>0.94</b>	<u>1.334</u>	1.802	<b>1.195</b>	<u>1.303</u>	1.812	<b>1.196</b>
eureka01	<u>0.94</u>	0.93	<b>0.97</b>	<u>2.081</u>	2.224	<b>1.427</b>	<u>1.436</u>	1.555	<b>1.171</b>
garmisch01	0.91	<u>0.93</u>	<b>0.96</b>	1.586	<u>1.569</u>	<b>1.019</b>	1.579	<u>1.354</u>	<b>1.010</b>
hefei01	0.88	<b>0.97</b>	<u>0.91</u>	1.447	<b>1.163</b>	<u>1.283</u>	1.450	<b>0.735</b>	<u>1.192</u>
izana01	<u>0.96</u>	0.88	<b>0.99</b>	<u>1.215</u>	1.413	<b>0.576</b>	<u>1.209</u>	1.417	<b>0.555</b>
jpl02	0.75	<b>0.89</b>	<u>0.76</u>	2.151	<b>1.146</b>	<u>1.525</u>	1.221	<b>0.885</b>	<u>1.174</u>
saga01	0.89	<b>0.95</b>	<u>0.94</u>	1.890	<b>1.087</b>	<u>1.263</u>	1.873	<b>1.090</b>	<u>1.254</u>
karlsruhe01	<u>0.89</u>	<b>0.93</b>	<b>0.93</b>	1.747	<b>1.327</b>	<u>1.375</u>	1.749	<b>1.318</b>	<u>1.376</u>
lauder02	<u>0.96</u>	0.89	<b>0.97</b>	1.213	<u>1.000</u>	<b>0.492</b>	<u>0.518</u>	0.993	<b>0.469</b>
lauder03	<b>0.94</b>	<u>0.72</u>	<b>0.94</b>	1.288	<u>1.064</u>	<b>0.565</b>	<u>0.863</u>	1.070	<b>0.538</b>
nicosia01	0.79	<u>0.91</u>	<b>0.94</b>	2.319	<b>0.731</b>	<u>0.862</u>	1.133	<u>0.661</u>	<b>0.641</b>
nyalesund01	<u>0.94</u>	0.93	<b>0.97</b>	<u>1.942</u>	2.233	<b>1.664</b>	<u>1.573</u>	1.707	<b>1.446</b>
lamont01	0.92	<b>0.97</b>	<u>0.96</u>	1.505	<b>0.956</b>	<u>0.964</u>	1.489	<b>0.794</b>	<u>0.929</u>
orleans01	0.92	<u>0.93</u>	<b>0.96</b>	1.450	<u>1.144</u>	<b>1.108</b>	1.361	<u>1.121</u>	<b>1.007</b>
parkfalls01	0.93	<b>0.96</b>	<u>0.95</u>	1.518	<u>1.210</u>	<b>1.160</b>	1.518	<u>1.211</u>	<b>1.160</b>
pasadena01	0.91	<u>0.93</u>	<b>0.95</b>	1.689	<u>1.543</u>	<b>1.382</b>	1.581	<u>1.329</u>	<b>1.160</b>
paris01	0.89	<u>0.92</u>	<b>0.93</b>	1.910	<b>1.418</b>	<u>1.451</u>	1.867	<b>1.433</b>	<u>1.437</u>
reunion01	<u>0.96</u>	<b>0.97</b>	<b>0.97</b>	1.276	<u>0.878</u>	<b>0.874</b>	<u>0.827</u>	0.886	<b>0.812</b>
rikubetsu01	0.90	<b>0.96</b>	<u>0.93</u>	1.688	<b>1.023</b>	<u>1.320</u>	1.667	<b>1.033</b>	<u>1.293</u>
sodankyla01	<u>0.94</u>	0.90	<b>0.97</b>	<u>1.539</u>	1.674	<b>1.241</b>	<u>1.427</u>	1.669	<b>1.232</b>
tsukuba02	0.92	<b>0.94</b>	<u>0.93</u>	1.429	<b>1.169</b>	<u>1.276</u>	1.322	<b>1.134</b>	<u>1.265</u>
xianghe01	0.61	<b>0.89</b>	<u>0.73</u>	2.513	<b>1.411</b>	<u>1.960</u>	2.487	<b>1.430</b>	<u>1.959</u>

251

252 **Table 5.** Metrics of the individual in-situ validation results for CAMS-EGG4, GOSAT, and fused XCH<sub>4</sub>. The best and second metrics are  
 253 denoted with bold and underlined fonts. CAMS: CAMS-EGG4; AF: after fusion. Unit: ppb for RMSE and  $\sigma$ .

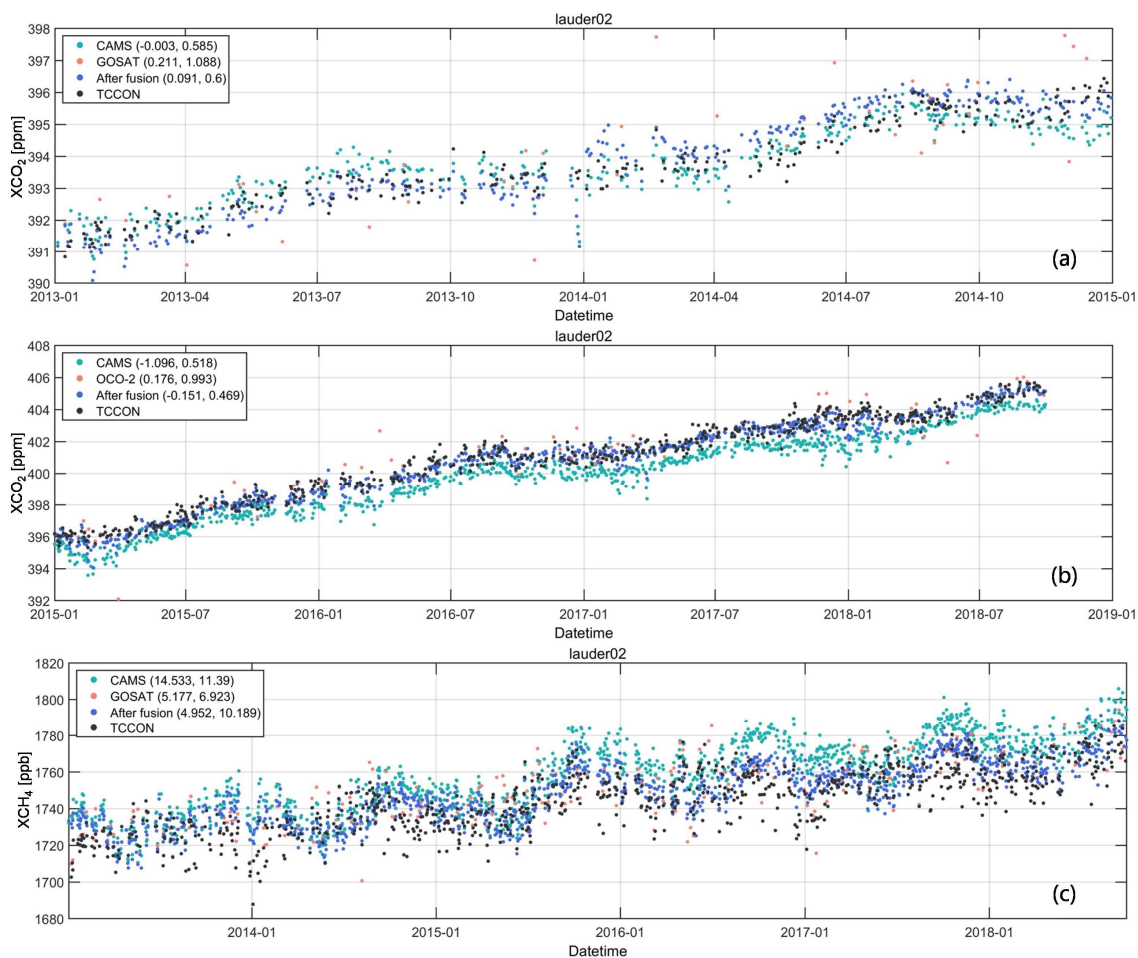
Site name	R <sup>2</sup>			RMSE			$\sigma$		
	CAMS	GOSAT	AF	CAMS	GOSAT	AF	CAMS	GOSAT	AF
bremen01	0.84	<b>0.90</b>	<u>0.87</u>	19.397	<u>15.328</u>	<b>14.969</b>	12.507	<b>9.868</b>	<u>10.938</u>
burgos01	<u>0.80</u>	<b>0.89</b>	<b>0.89</b>	10.981	<u>10.455</u>	<b>8.096</b>	9.194	<b>6.136</b>	<u>7.216</u>
edwards01	0.83	<u>0.88</u>	<b>0.89</b>	15.170	<u>13.413</u>	<b>11.173</b>	9.960	<u>9.099</u>	<b>8.049</b>
fourcorners01	0.40	<b>0.71</b>	<u>0.51</u>	14.732	<b>7.714</b>	<u>9.847</u>	9.711	<b>6.710</b>	<u>8.777</u>
garmisch01	0.83	<u>0.85</u>	<b>0.89</b>	16.693	<u>13.258</u>	<b>12.267</b>	<u>11.568</u>	11.643	<b>9.577</b>
hefei01	0.54	<u>0.56</u>	<b>0.66</b>	22.072	<b>15.377</b>	<u>16.814</u>	16.165	<b>13.370</b>	<u>13.826</u>
jpl02	0.81	<b>0.88</b>	<u>0.86</u>	16.989	<b>9.679</b>	<u>9.788</u>	11.288	<b>8.840</b>	<u>9.604</u>
saga01	0.85	<b>0.92</b>	<u>0.89</u>	11.299	<b>9.089</b>	<u>9.311</u>	10.091	<b>8.422</b>	<u>9.147</u>
karlsruhe01	0.70	<u>0.80</u>	<b>0.81</b>	13.688	<u>11.913</u>	<b>10.042</b>	11.564	<u>11.370</u>	<b>9.177</b>
lauder02	<u>0.66</u>	<b>0.84</b>	0.65	18.460	<b>8.632</b>	<u>11.323</u>	11.390	<b>6.923</b>	<u>10.189</u>
lauder03	0.46	<b>0.76</b>	<u>0.57</u>	16.568	<b>8.531</b>	<u>12.166</u>	10.965	<b>6.491</b>	<u>9.347</u>
lamont01	0.82	<b>0.94</b>	<u>0.88</u>	<u>11.762</u>	12.204	<b>9.497</b>	11.494	<b>7.015</b>	<u>9.460</u>
orleans01	<u>0.80</u>	<b>0.88</b>	<b>0.88</b>	18.341	<u>13.734</u>	<b>13.305</b>	12.038	<u>9.690</u>	<b>9.395</b>
parkfalls01	0.79	<b>0.87</b>	<u>0.84</u>	17.107	<u>14.892</u>	<b>13.784</b>	13.396	<b>10.548</b>	<u>11.519</u>
pasadena01	0.82	<b>0.90</b>	<u>0.88</u>	12.658	<b>8.396</b>	<u>8.845</u>	10.544	<b>8.094</b>	<u>8.802</u>
paris01	<u>0.75</u>	0.73	<b>0.84</b>	<u>12.313</u>	13.077	<b>9.578</b>	<u>10.319</u>	11.437	<b>8.383</b>
reunion01	<u>0.51</u>	0.41	<b>0.73</b>	18.245	<u>13.846</u>	<b>10.092</b>	<u>10.221</u>	11.427	<b>7.432</b>
rikubetsu01	0.60	<b>0.81</b>	<u>0.72</u>	21.166	<u>20.160</u>	<b>18.250</b>	15.263	<b>11.481</b>	<u>12.759</u>
sodankyla01	<u>0.84</u>	0.83	<b>0.87</b>	23.494	<b>15.701</b>	<u>18.806</u>	<u>12.164</u>	12.682	<b>10.917</b>
tsukuba02	0.77	<b>0.86</b>	<u>0.83</u>	11.726	<b>8.165</b>	<u>8.704</u>	9.401	<b>7.623</b>	<u>8.424</u>
xianghe01	<u>0.63</u>	<b>0.69</b>	<u>0.63</u>	<b>14.851</b>	15.840	<u>15.266</u>	<u>14.734</u>	<b>13.752</b>	14.736



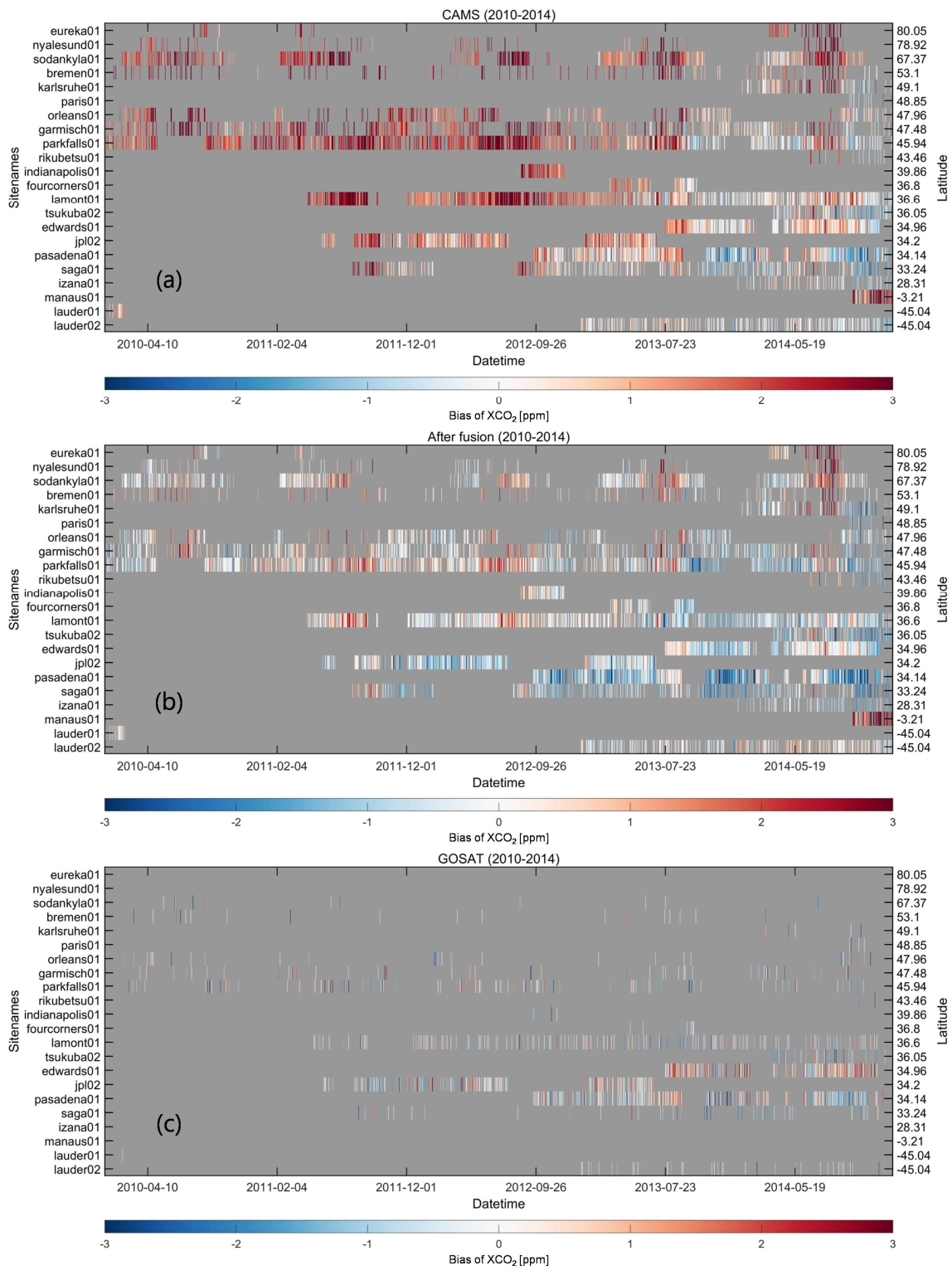
254 **Figure 6.** Scatter-plots of the time series for daily CAMS-EGG4, GOSAT, OCO-2, fused, and TCCON data on garmisch01. The first and  
 255 second numbers in the bracket represent  $\mu$  and  $\sigma$ , respectively. Unit: ppm/ppb to XCO<sub>2</sub>/XCH<sub>4</sub> for  $\mu$  and  $\sigma$ .  
 256

257 **4.2 Individual in-situ validation and time series**

258 Figure 4, 5, and Table 3-5 show the individual in-situ validation results for the CAMS-EGG4, GOSAT, OCO-2, and fused  
 259 results on each TCCON in-situ station. It is worth noting that only the stations where the individual validation results are  
 260 significant ( $p$ -level  $< 0.01$ ) for all datasets (i.e., CAMS-EGG4, GOSAT, OCO-2, and the fused results) are presented. Since  
 261 the space of text is limited, two stations named edwards01 and sodankyla01 are selected as examples (see Fig. 4 and 5), which  
 262 locate in North America and Europe, respectively. As can be seen, the fused results achieve the best performance compared to  
 263 CAMS-EGG4, GOSAT, and OCO-2 on edwards01 and sodankyla01, with the  $R^2$  ranging from 0.87 to 0.97. Especially, the  
 264 large overestimation of  $XCO_2$  for CAMS-EGG4 on sodankyla01 ( $\mu = 2.071$  ppm) is well mitigated after fusion ( $\mu = 0.377$   
 265 ppm), even for the poor data availability of GOSAT ( $N = 11$ ). This indicates the strong universality of the proposed fusion  
 266 method. The valid individual validation results on all stations are given in Table 3-5. It can be observed that the performance  
 267 of the fused results exceeds those of CAMS-EGG4 and GOSAT/OCO-2 for almost all stations and  $\sim 70\%$  of stations,  
 268 respectively.

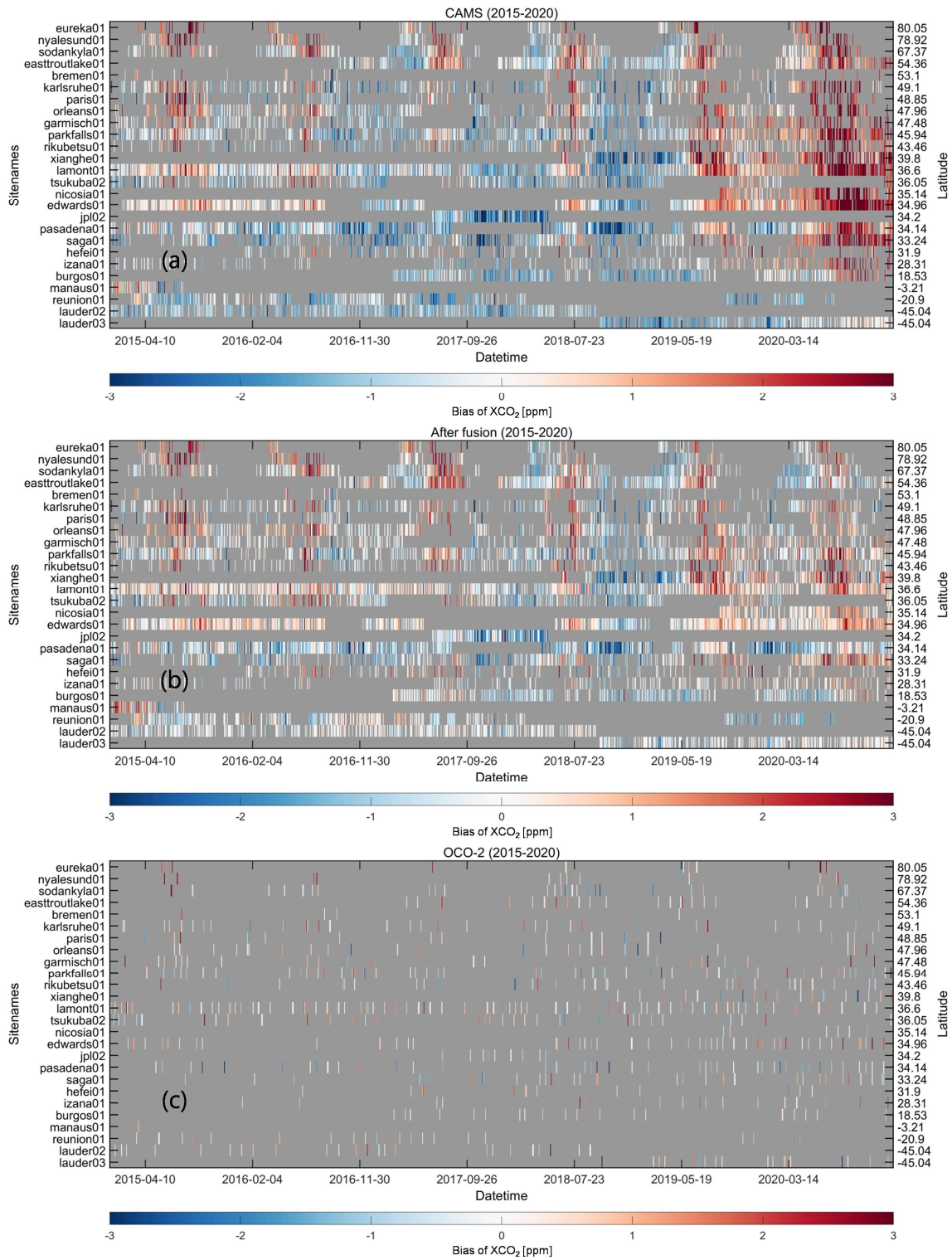


269  
 270 **Figure 7.** Scatter-plots of the time series for daily CAMS-EGG4, GOSAT, OCO-2, fused, and TCCON data on lauder02. The first and second  
 271 numbers in the bracket represent  $\mu$  and  $\sigma$ , respectively. Unit: ppm/ppb to  $XCO_2/XCH_4$  for  $\mu$  and  $\sigma$ .



272

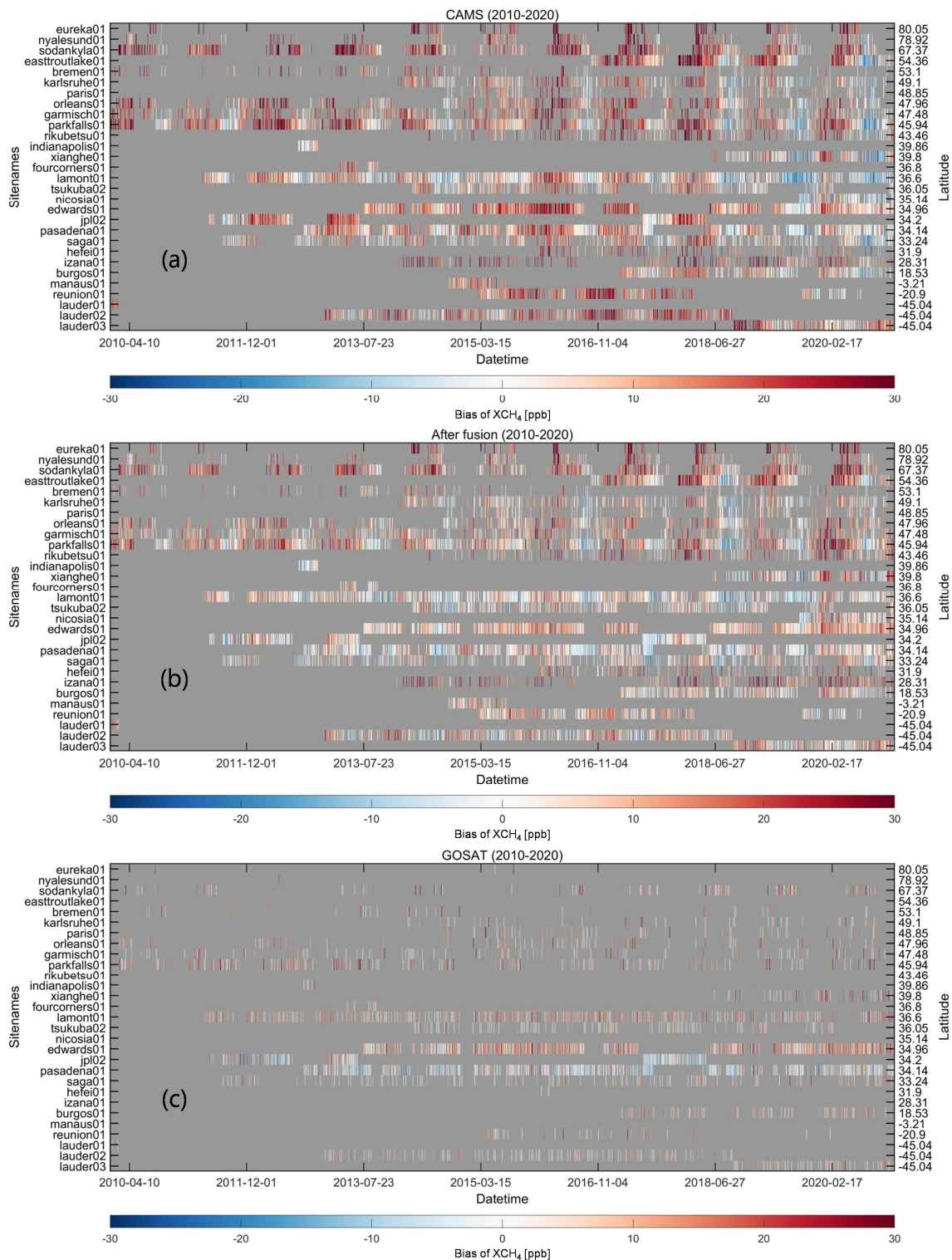
273 **Figure 8.** Heat maps of the biases between daily (a) CAMS-EGG4/(b) fused/(c) GOSAT and TCCON XCO<sub>2</sub> over time and latitude. Color  
 274 ramps stand for the biases of XCO<sub>2</sub>. Background colors (grey) indicate the missing data.



275

276 **Figure 9.** Heat maps of the biases between daily (a) CAMS-EGG4/(b) fused/(c) OCO-2 and TCCON XCO<sub>2</sub> over time and latitude. Color  
 277 ramps stand for the biases of XCO<sub>2</sub>. Background colors (grey) indicate the missing data.



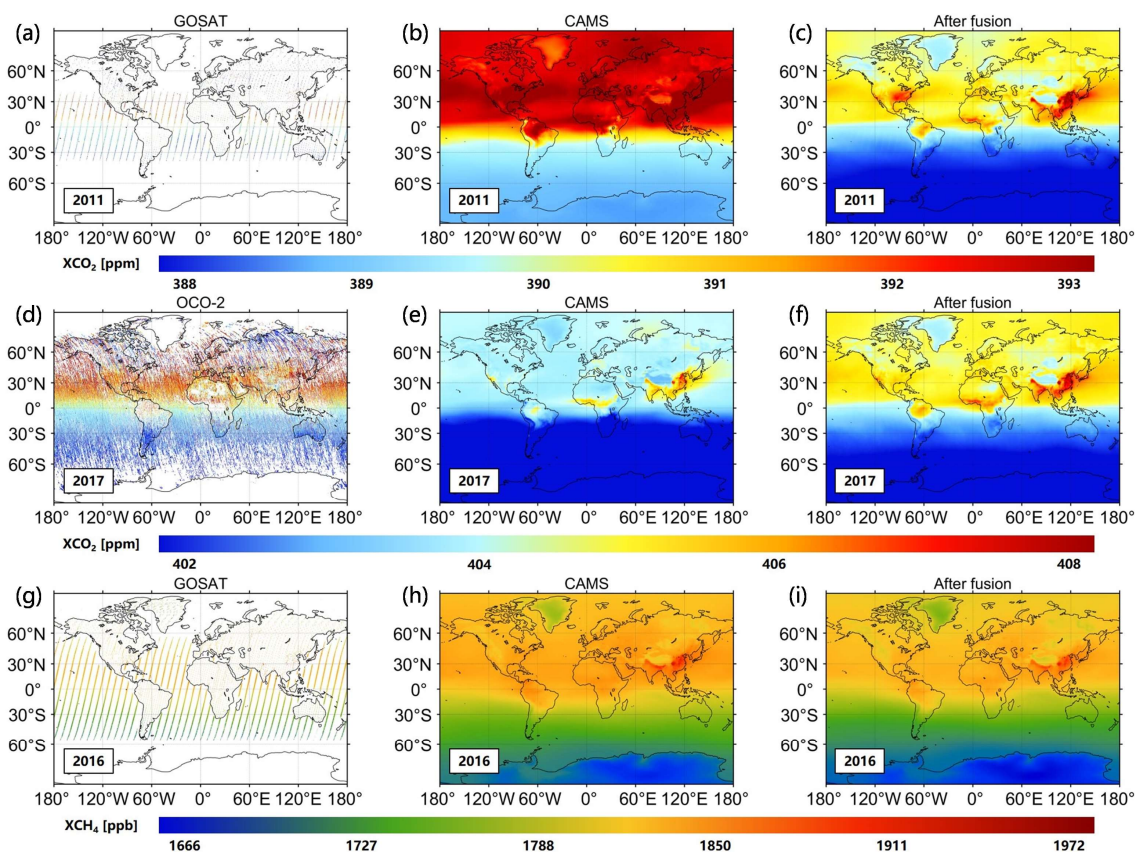


278

279 **Figure 10.** Heat maps of the biases between daily (a) CAMS-EGG4/(b) fused/(c) GOSAT and TCCON XCH<sub>4</sub> over time and latitude. Color  
 280 ramps stand for the biases of XCO<sub>2</sub>. Background colors (grey) indicate the missing data.

281 Figure 6 and 7 demonstrate the time series for daily CAMS-EGG4, GOSAT, OCO-2, fused, and TCCON data on individual  
 282 in-situ stations. Similarly, two stations, i.e., garmisch01 and lauder02, are regarded as examples, which locate in Europe and  
 283 Oceania, respectively. As depicted in Fig. 6, the XCO<sub>2</sub> from CAMS-EGG4 is markedly overestimated on garmisch01 from  
 284 2010 to 2014 and in 2020. After fusion, the XCO<sub>2</sub> presents an equal trend compared to TCCON measurements over time, with  
 285 smaller  $\mu$  (0.096 and 0.139 ppm) and  $\sigma$  (1.067 and 1.01 ppm). In the meantime, the overestimation of CAMS-EGG4 XCH<sub>4</sub>

286 is also mitigated on garmisch01 through our fusion method. Regarding lauder02, Figure 7 shows that CAMS-EGG4 generates  
 287 underestimated XCO<sub>2</sub> (2015-2019) and overestimated XCH<sub>4</sub>. The  $\mu$  and  $\sigma$  of the fused results (e.g., 4.952 and 10.189 ppb  
 288 for XCH<sub>4</sub>) are significantly improved on lauder02.

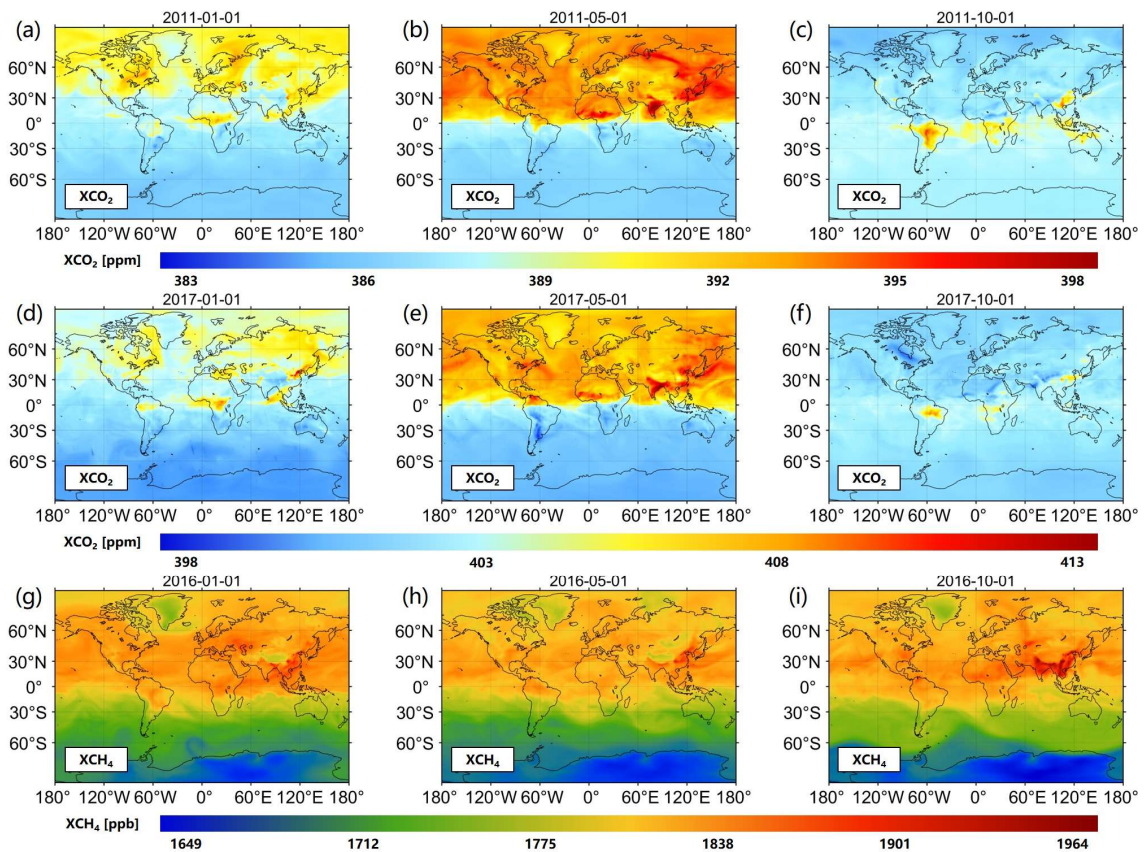


289  
 290 **Figure 11.** Annual (a and g) GOSAT, (d) OCO-2, (b, e, and h) CAMS-EGG4, and (c, f, and i) fused XCO<sub>2</sub>/XCH<sub>4</sub> over the globe. Color  
 291 ramps stand for the values of XCO<sub>2</sub> and XCH<sub>4</sub>.

### 292 4.3 Uncertainty analyses

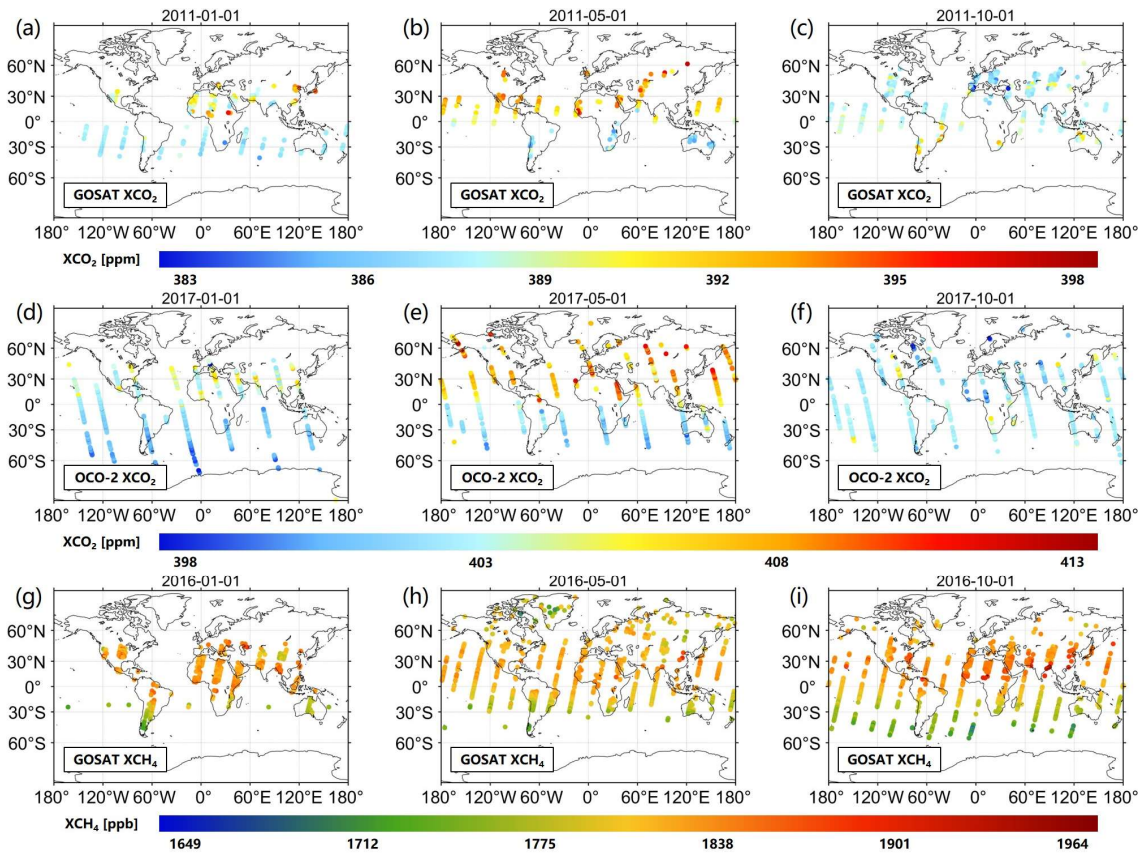
293 Figure 8-10 display the biases between daily CAMS-EGG4/fused/GOSAT/OCO-2 and TCCON data over time and latitude.  
 294 As observed in Fig. 8 and 9, a large overestimation generally exists in the CAMS-EGG4 XCO<sub>2</sub> from 2010 to 2014 and in 2020,  
 295 especially before 2013 and in 2020 (> 3 ppm). These are attributed to the considerable errors in the satellite data assimilated  
 296 (2010-2014) and that anthropogenic emissions are not modified for COVID-19 lockdowns in 2020 (Agusti-Panareda et al.,  
 297 2022). After fusion, the biases of XCO<sub>2</sub> are well improved for most TCCON in-situ stations from 2010 to 2014 and in 2020,  
 298 whose patterns are similar to those of GOSAT and OCO-2 XCO<sub>2</sub>, respectively. This indicates that the proposed fusion method  
 299 can effectively correct the biases in CAMS-EGG4 due to the issues from assimilation data. Meanwhile, CAMS-EGG4  
 300 generates distinctly underestimated XCO<sub>2</sub> from 2016 to 2019 on the stations of latitude < 40° N, which is also mitigated via  
 301 the S-STDCT fusion method (see Fig. 10). Moreover, the CAMS-EGG4 XCH<sub>4</sub> frequently presents a large positive bias (> 30  
 302 ppb), while the fused XCH<sub>4</sub> only enhances the performance on the stations of latitude < 50° N. The improvements for other  
 303 stations require our further efforts in the future.





304

305 **Figure 12.** Daily fused (a-f) XCO<sub>2</sub> and (g-i) XCH<sub>4</sub> over the globe. Color ramps stand for the values of XCO<sub>2</sub> and XCH<sub>4</sub>.



306

307 **Figure 13.** Daily (a-c) GOSAT, (d-f) OCO-2 XCO<sub>2</sub>, and (g-i) GOSAT XCH<sub>4</sub> over the globe. Color ramps stand for the values of XCO<sub>2</sub> and  
308 XCH<sub>4</sub>.

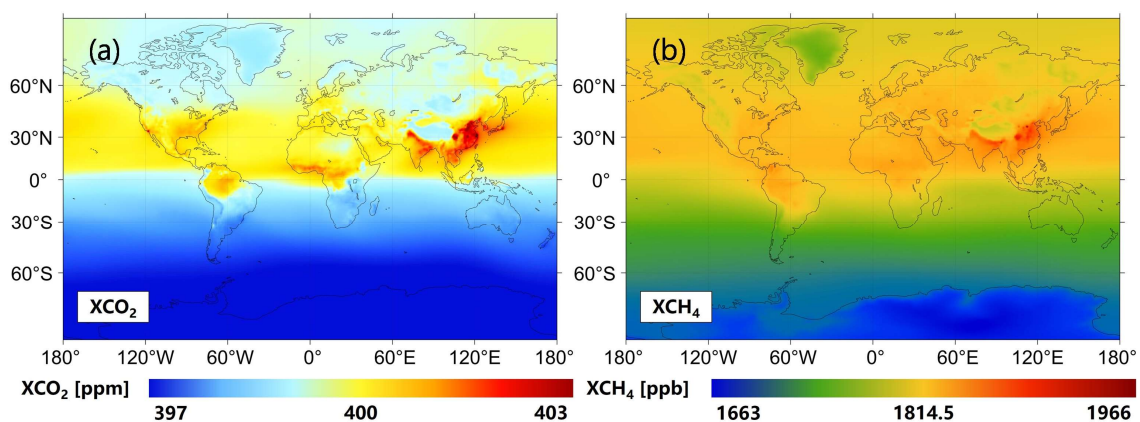
#### 309 4.4 Assessment of spatial distribution on multi-temporal scales

310 Figure 11 demonstrates the comparisons of annual GOSAT, OCO-2, CAMS-EGG4, and fused XCO<sub>2</sub>/XCH<sub>4</sub> over the globe. A  
311 total of three years are selected, including 2011, 2017, and 2016. As can be seen, the fused results present coincident spatial  
312 patterns with GOSAT and OCO-2, even if the annual GOSAT and OCO-2 data are greatly sparse. Particularly, the large  
313 overestimation and underestimation of CAMS-EGG4 XCO<sub>2</sub> in 2011 and 2017 are significantly modified after fusion,  
314 respectively, which are mutually confirmed with the descriptions in Section 4.3.

315 Figure 12 illustrates the examples of daily fused XCO<sub>2</sub> and XCH<sub>4</sub> over the globe, consisting of three days in three years. As  
316 shown, the fused results display detailed information on atmospheric CO<sub>2</sub> and CH<sub>4</sub>, which clearly indicate their regional and  
317 global spatial patterns. In addition, incoherent or factitious spatial distribution is not observed in the fused XCO<sub>2</sub> and XCH<sub>4</sub>.

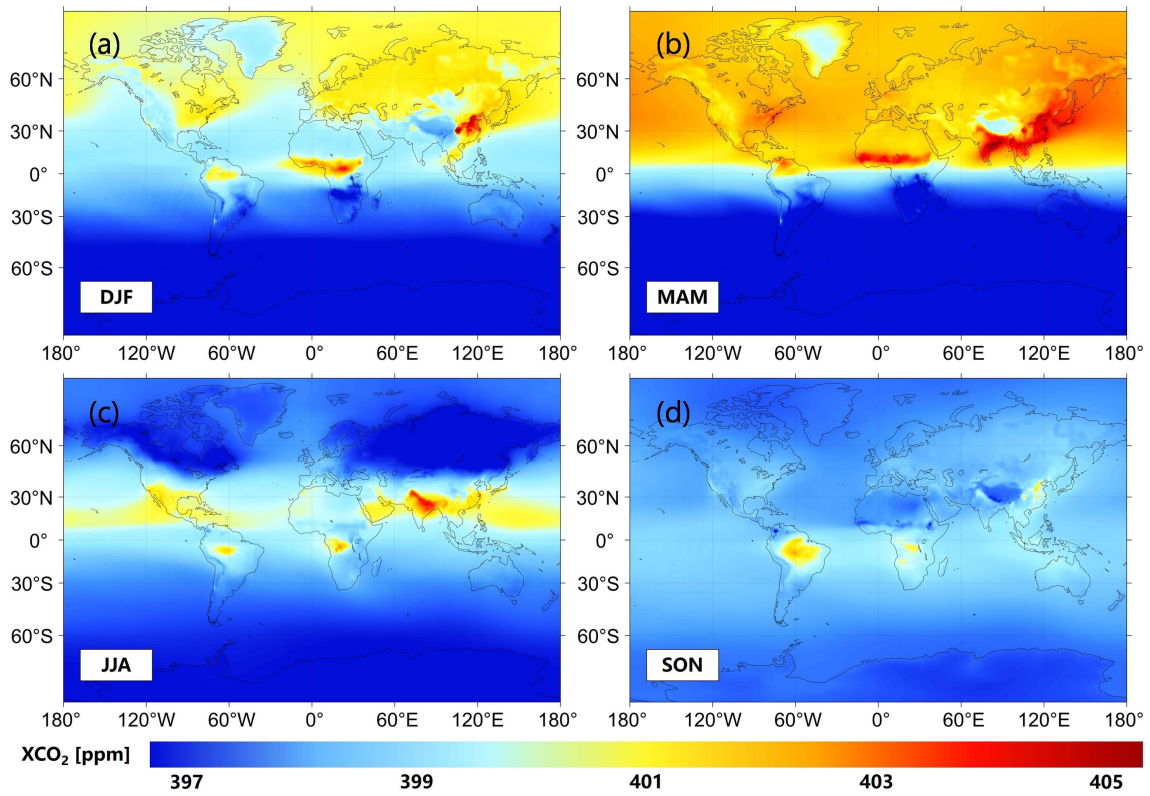
318 Figure 13 then provides the corresponding daily XCO<sub>2</sub> and XCH<sub>4</sub> from GOSAT and OCO-2 over the globe. It is worth noting  
319 that the daily satellite XCO<sub>2</sub> and XCH<sub>4</sub> are mapped via footprints due to their significant sparse coverage, which are nearly  
320 invisible at grids of 0.25°. As expected, the fused results present identical spatial distribution compared to XCO<sub>2</sub> and XCH<sub>4</sub>  
321 from GOSAT and OCO-2. This suggests the robustness and reliability of the proposed fusion method.

322 Figure 14 depicts the multi-year mean fused global XCO<sub>2</sub> and XCH<sub>4</sub> from 2010 to 2020. Generally, the spatial patterns of  
323 XCO<sub>2</sub> and XCH<sub>4</sub> are divided by the equator. The high values of XCO<sub>2</sub> and XCH<sub>4</sub> mainly distribute over Asia, e.g., China and  
324 India, which is attributed to the large anthropogenic emissions (Kenea et al., 2023; Liu et al., 2020; Turner et al., 2015;  
325 Hotchkiss et al., 2015). In the meantime, considerable natural emissions, e.g., wildfires (Arora and Melton, 2018), also can  
326 obviously increase the XCO<sub>2</sub> values, such as in central Africa and northern South America. Figure 15 and 16 illustrate the  
327 seasonal fused XCO<sub>2</sub> and XCH<sub>4</sub> from 2010 to 2020 over the globe, respectively. As displayed, seasonal changes of global  
328 XCO<sub>2</sub> and XCH<sub>4</sub> spatial patterns are clearly reflected in the fused results. Compared to XCH<sub>4</sub>, the global spatial patterns of  
329 XCO<sub>2</sub> vary more drastically. This is likely driven by the spatiotemporal heterogeneity of meteorological fields (Liu et al., 2011)  
330 and different emission sources of CO<sub>2</sub> and CH<sub>4</sub>.



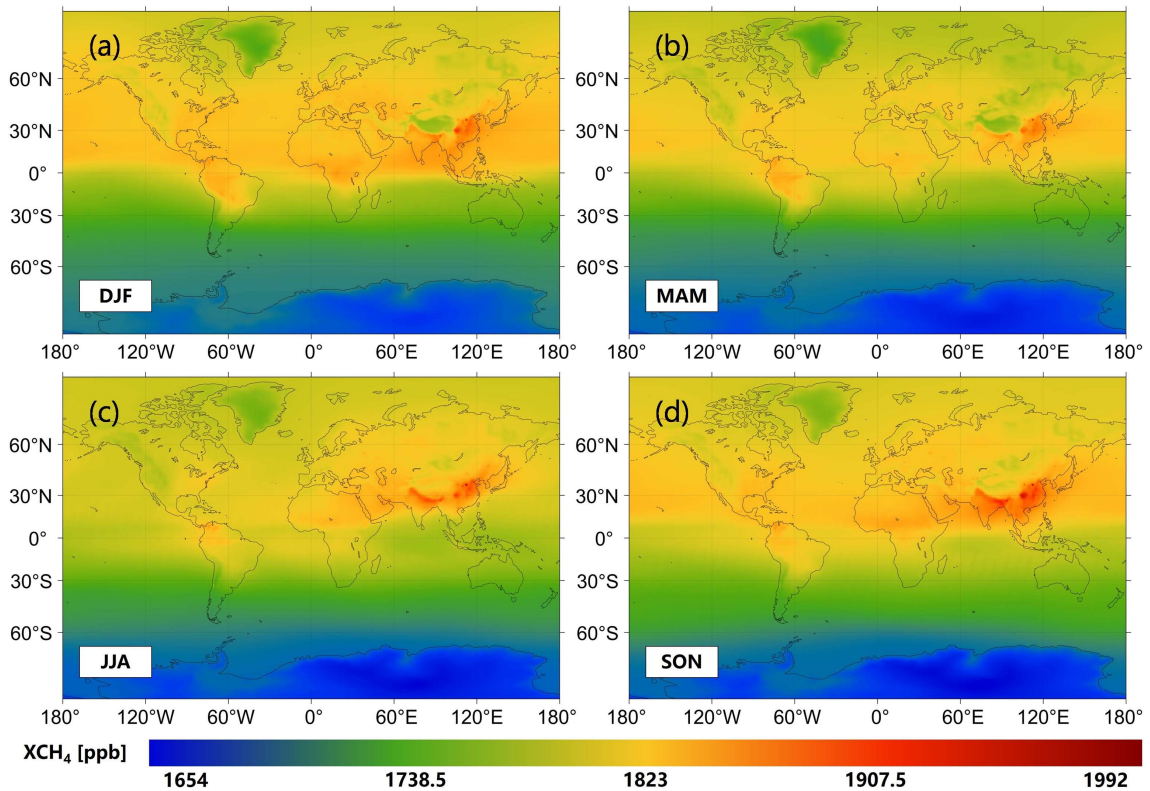
331  
332 **Figure 14.** Multi-year mean fused (a) XCO<sub>2</sub> and (b) XCH<sub>4</sub> from 2010 to 2020 over the globe. Color ramps stand for the values of XCO<sub>2</sub> and  
333 XCH<sub>4</sub>.





334

335 **Figure 15.** Seasonal fused XCO<sub>2</sub> from 2010 to 2020 over the globe. The color ramp stands for the value of XCO<sub>2</sub>. (a) DJF, (b) MAM, (c)  
 336 JJA, and (d) SON denote Dec. to Feb., Mar. to May., Jun. to Aug., and Sep. to Nov., respectively.



337

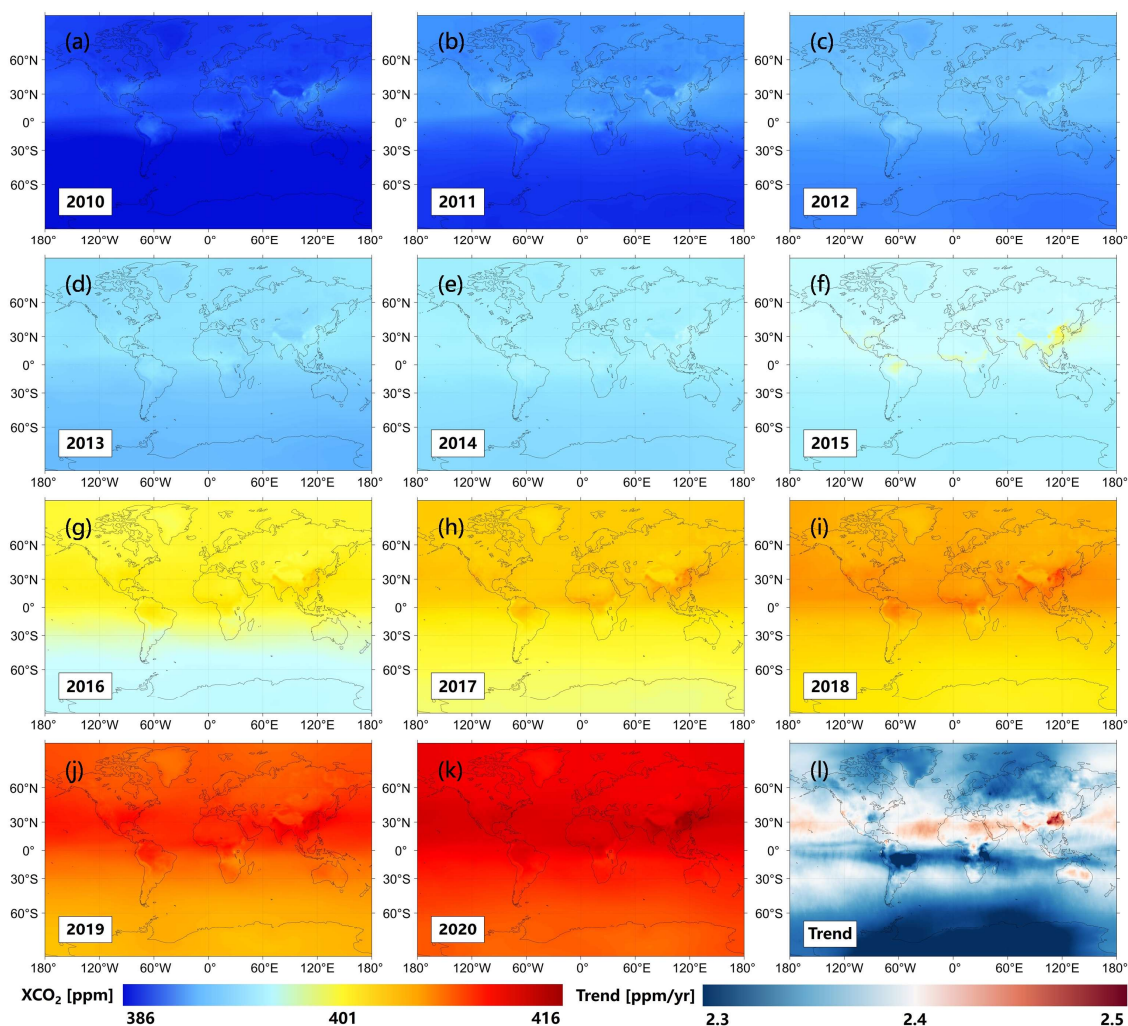
338 **Figure 16.** Seasonal fused XCH<sub>4</sub> from 2010 to 2020 over the globe. The color ramp stands for the value of XCH<sub>4</sub>. (a) DJF, (b) MAM, (c)  
 339 JJA, and (d) SON denote Dec. to Feb., Mar. to May., Jun. to Aug., and Sep. to Nov., respectively.

340 Figure 17 and 18 map the annual fused global XCO<sub>2</sub> and XCH<sub>4</sub> from 2010 to 2020, respectively, including their trends. As

341 observed in Fig. 17, the CO<sub>2</sub> levels continuously increase from 2010 to 2020, with the mean XCO<sub>2</sub> values ranging from ≤  
 342 386 to ≥ 416 ppm. However, the trends of XCO<sub>2</sub> only present small spatial differences (~ 0.2 ppm per year), of which the  
 343 large growth rates primarily distribute along the equator, especially for China (≥ 2.5 ppm per year). It is worth noting that the  
 344 growth rates of XCO<sub>2</sub> are relatively slight (≤ 2.3 ppm per year) in northern South America compared to other regions. This is  
 345 likely caused by the effects from the carbon sequestration of forests (Chazdon et al., 2016). Besides, the XCH<sub>4</sub> values also  
 346 notably rise from 2010 to 2020, of which the maximum is not less than 2008 ppb in 2020 (see Fig. 18). The large growth rates  
 347 of XCH<sub>4</sub> are majorly discovered over southern Asia and northern Europe.

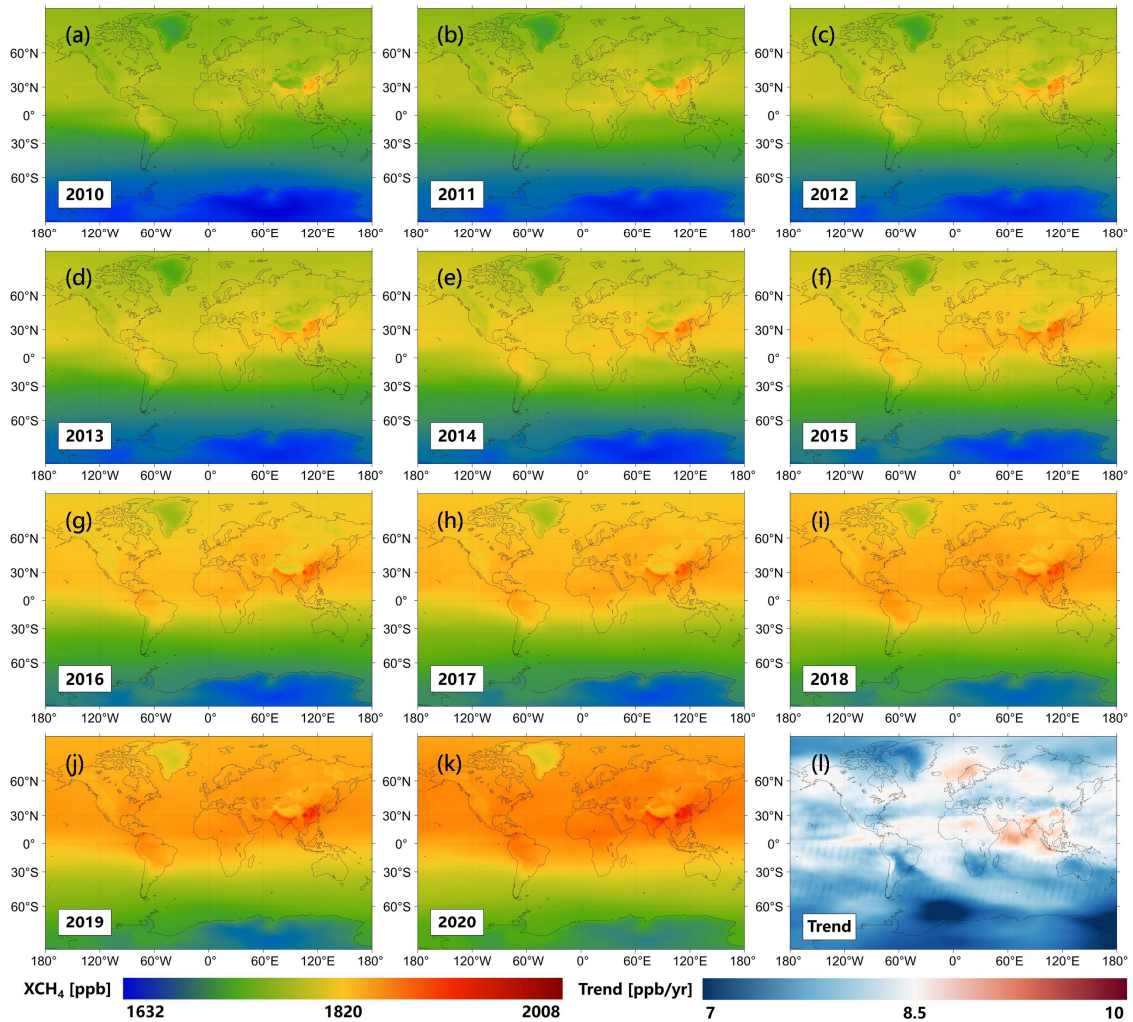
## 348 5 Data availability

349 The fused results can be freely accessed at <http://doi.org/10.5281/zenodo.7388893> (Wang et al., 2022b). The daily global  
 350 seamless gridded (0.25°) XCO<sub>2</sub> and XCH<sub>4</sub> from 2010 to 2020 are stored in the netCDF4 format with a file size of ~ 3.5 MB  
 351 for each day. The units of XCO<sub>2</sub> and XCH<sub>4</sub> are ppm and ppb, respectively.



352  
 353 **Figure 17.** Annual fused (a-k) XCO<sub>2</sub> and (l) its trend from 2010 to 2020 over the globe. Color ramps stand for the values of XCO<sub>2</sub> and its  
 354 trend. ppm/yr: ppm per year.





355  
 356 **Figure 18.** Annual fused (a-k) XCH<sub>4</sub> and (l) its trend from 2010 to 2020 over the globe. Color ramps stand for the values of XCH<sub>4</sub> and its  
 357 trend. ppb/yr: ppb per year.

## 358 6 Conclusions

359 In our study, a novel spatiotemporally self-supervised fusion method, i.e., S-STDCT, is proposed to acquire long-term daily  
 360 seamless globally distributed XCO<sub>2</sub> and XCH<sub>4</sub> products from 2010 to 2020 at the grids of 0.25°. A total of three datasets are  
 361 adopted, which include GOSAT, OCO-2, and CAMS-EGG4. Since the data from GOSAT and OCO-2 is greatly sparse in  
 362 space-time domain, the algorithm for frequency domain (the *STDCT*) is applied in the fusion task. Validation results show that  
 363 the S-STDCT fusion method performs well over the globe, with the  $\sigma$  of  $\sim 1.18$  ppm for XCO<sub>2</sub> and 11.3 ppb for XCH<sub>4</sub> against  
 364 TCCON measurements during 2010-2020. Meanwhile, the R<sup>2</sup> of fused XCO<sub>2</sub> and XCH<sub>4</sub> reach 0.91/0.95 (2010-2014/2015-  
 365 2020) and 0.9 (2010-2020), respectively. Generally, the accuracy of fused results is distinctly superior to that of CAMS-EGG4,  
 366 which also exceeds or equals those of GSOAT and OCO-2. Particularly, the proposed fusion method effectively modifies the  
 367 large biases in CAMS-EGG4 caused by the issues from assimilation data, such as the uncorrected anthropogenic emission  
 368 inventories for COVID-19 lockdowns in 2020. Besides, the spatial patterns of fused results remain coincident with GOSAT  
 369 and OCO-2, which can accurately display the long-term and seasonal changes of global XCO<sub>2</sub> and XCH<sub>4</sub> spatial distribution.

370 The long-term (2010-2020) daily global seamless gridded (0.25°) fused results are available at  
371 <http://doi.org/10.5281/zenodo.7388893> (Wang et al., 2022b).

372 Overall, the developed fusion method generates high-quality full-coverage XCO<sub>2</sub> and XCH<sub>4</sub> datasets over the globe from 2010  
373 to 2020. However, it only considers the global spatiotemporal knowledge of self-correlation in GOSAT and OCO-2 products  
374 without attention to local spatiotemporal information. Meanwhile, the spatial resolution and available period of fused results  
375 should be further enhanced, which are devised as 0.1° and more than 20 years (e.g., 2000-2020), respectively. To fix these  
376 issues, we will spare no effort to work on our future works.

### 377 **Author contributions**

378 YW designed the study, collected and processed the data, analyzed the results, and wrote the paper. QQY and TWL provided  
379 constructive comments on the paper. YJY, SQZ, and LPZ revised the paper. All authors contributed to the study.

### 380 **Competing interests**

381 The contact author has declared that none of the authors has any competing interests.

### 382 **Disclaimer**

383 Publisher's note: Copernicus Publications remains neutral with regard to jurisdictional claims in published maps and  
384 institutional affiliations.

### 385 **Acknowledgments**

386 The authors would like to express gratitude to the Goddard Earth Science Data and Information Services Center for providing  
387 the GOSAT and OCO-2 XCO<sub>2</sub> products (last access: 20 November 2022 and 27 November 2022), the Centre for  
388 Environmental Data Analysis for providing the GOSAT XCH<sub>4</sub> product (last access: 18 November 2022), the Copernicus  
389 Climate Data Store for providing the CAMS-EGG4 XCO<sub>2</sub> and XCH<sub>4</sub> products (last access: 25 November 2022), the Total  
390 Carbon Column Observing Network (hosted by CaltechDATA at <https://tcocondata.org>; Chair: Dr. Debra Wunch) for  
391 establishing and maintaining in-situ stations (last access: 18 November 2022).

### 392 **Financial support**

393 Our work is supported by the National Key R&D Program of China (2022YFB3903403) and the Basic and Applied Basic  
394 Research Foundation of Guangdong Province (No. 2021A1515110567).

- 396 Agusti-Panareda, A., Barré, J., Massart, S., Inness, A., Aben, I., Ades, M., Baier, B. C., Balsamo, G., Borsdorff, T.,  
397 Bousseret, N., Boussetta, S., Buchwitz, M., Cantarello, L., Crevoisier, C., Engelen, R., Eskes, H., Flemming, J.,  
398 Garrigues, S., Hasekamp, O., Huijnen, V., Jones, L., Kipling, Z., Langerock, B., McNorton, J., Meilhac, N., Noel, S.,  
399 Parrington, M., Peuch, V.-H., Ramonet, M., Ratzinger, M., Reuter, M., Ribas, R., Suttie, M., Sweeney, C., Tarniewicz,  
400 J., and Wu, L.: Technical note: The CAMS greenhouse gas reanalysis from 2003 to 2020, *EGUsphere*, 1–51,  
401 <https://doi.org/10.5194/egusphere-2022-283>, 2022.
- 402 Arora, V. K. and Melton, J. R.: Reduction in global area burned and wildfire emissions since 1930s enhances carbon  
403 uptake by land, *Nat Commun*, 9, 1326, <https://doi.org/10.1038/s41467-018-03838-0>, 2018.
- 404 August, T., Klaes, D., Schlüssel, P., Hultberg, T., Crapeau, M., Arriaga, A., O’Carroll, A., Coppens, D., Munro, R., and  
405 Calbet, X.: IASI on Metop-A: Operational Level 2 retrievals after five years in orbit, *Journal of Quantitative*  
406 *Spectroscopy and Radiative Transfer*, 113, 1340–1371, <https://doi.org/10.1016/j.jqsrt.2012.02.028>, 2012.
- 407 Battin, T. J., Luysaert, S., Kaplan, L. A., Aufdenkampe, A. K., Richter, A., and Tranvik, L. J.: The boundless carbon  
408 cycle, *Nature Geosci*, 2, 598–600, <https://doi.org/10.1038/ngeo618>, 2009.
- 409 Beirle, S., Lampel, J., Wang, Y., Mies, K., Dörner, S., Grossi, M., Loyola, D., Dehn, A., Danielczok, A., Schröder, M.,  
410 and Wagner, T.: The ESA GOME-Evolution “Climate” water vapor product: a homogenized time series of H<sub>2</sub>O columns  
411 from GOME, SCIAMACHY, and GOME-2, *Earth System Science Data*, 10, 449–468, [https://doi.org/10.5194/essd-10-](https://doi.org/10.5194/essd-10-449-2018)  
412 [449-2018](https://doi.org/10.5194/essd-10-449-2018), 2018.
- 413 Bergamaschi, P., Houweling, S., Segers, A., Krol, M., Frankenberg, C., Scheepmaker, R. A., Dlugokencky, E., Wofsy, S.  
414 C., Kort, E. A., Sweeney, C., Schuck, T., Brenninkmeijer, C., Chen, H., Beck, V., and Gerbig, C.: Atmospheric CH<sub>4</sub> in  
415 the first decade of the 21st century: Inverse modeling analysis using SCIAMACHY satellite retrievals and NOAA surface  
416 measurements, *Journal of Geophysical Research: Atmospheres*, 118, 7350–7369, <https://doi.org/10.1002/jgrd.50480>,  
417 2013.
- 418 Bhattacharjee, S., Mitra, P., and Ghosh, S. K.: Spatial Interpolation to Predict Missing Attributes in GIS Using Semantic  
419 Kriging, *IEEE Transactions on Geoscience and Remote Sensing*, 52, 4771–4780,  
420 <https://doi.org/10.1109/TGRS.2013.2284489>, 2014.
- 421 Buchwitz, M., Reuter, M., Schneising, O., Boesch, H., Guerlet, S., Dils, B., Aben, I., Armante, R., Bergamaschi, P.,  
422 Blumenstock, T., Bovensmann, H., Brunner, D., Buchmann, B., Burrows, J. P., Butz, A., Chédin, A., Chevallier, F.,  
423 Crevoisier, C. D., Deutscher, N. M., Frankenberg, C., Hase, F., Hasekamp, O. P., Heymann, J., Kaminski, T., Laeng, A.,  
424 Lichtenberg, G., De Mazière, M., Noël, S., Notholt, J., Orphal, J., Popp, C., Parker, R., Scholze, M., Sussmann, R., Stiller,  
425 G. P., Warneke, T., Zehner, C., Bril, A., Crisp, D., Griffith, D. W. T., Kuze, A., O’Dell, C., Oshchepkov, S., Sherlock, V.,  
426 Suto, H., Wennberg, P., Wunch, D., Yokota, T., and Yoshida, Y.: The Greenhouse Gas Climate Change Initiative (GHG-  
427 CCD): Comparison and quality assessment of near-surface-sensitive satellite-derived CO<sub>2</sub> and CH<sub>4</sub> global data sets,  
428 *Remote Sensing of Environment*, 162, 344–362, <https://doi.org/10.1016/j.rse.2013.04.024>, 2015.
- 429 Burrows, J. P., Hölzle, E., Goede, A. P. H., Visser, H., and Fricke, W.: SCIAMACHY—scanning imaging absorption  
430 spectrometer for atmospheric cartography, *Acta Astronautica*, 35, 445–451, [https://doi.org/10.1016/0094-](https://doi.org/10.1016/0094-5765(94)00278-T)  
431 [5765\(94\)00278-T](https://doi.org/10.1016/0094-5765(94)00278-T), 1995.
- 432 Chazdon, R. L., Broadbent, E. N., Rozendaal, D. M. A., Bongers, F., Zambrano, A. M. A., Aide, T. M., Balvanera, P.,  
433 Becknell, J. M., Boukili, V., Brancalion, P. H. S., Craven, D., Almeida-Cortez, J. S., Cabral, G. A. L., de Jong, B.,



434 Denslow, J. S., Dent, D. H., DeWalt, S. J., Dupuy, J. M., Durán, S. M., Espírito-Santo, M. M., Fandino, M. C., César, R.  
435 G., Hall, J. S., Hernández-Stefanoni, J. L., Jakovac, C. C., Junqueira, A. B., Kennard, D., Letcher, S. G., Lohbeck, M.,  
436 Martínez-Ramos, M., Massoca, P., Meave, J. A., Mesquita, R., Mora, F., Muñoz, R., Muscarella, R., Nunes, Y. R. F.,  
437 Ochoa-Gaona, S., Orihuela-Belmonte, E., Peña-Claros, M., Pérez-García, E. A., Piotto, D., Powers, J. S., Rodríguez-  
438 Velazquez, J., Romero-Pérez, I. E., Ruiz, J., Saldarriaga, J. G., Sanchez-Azofeifa, A., Schwartz, N. B., Steininger, M. K.,  
439 Swenson, N. G., Uriarte, M., van Breugel, M., van der Wal, H., Veloso, M. D. M., Vester, H., Vieira, I. C. G., Bentos, T.  
440 V., Williamson, G. B., and Poorter, L.: Carbon sequestration potential of second-growth forest regeneration in the Latin  
441 American tropics, *Science Advances*, 2, e1501639, <https://doi.org/10.1126/sciadv.1501639>, 2016.

442 Chen, H., Xu, X., Fang, C., Li, B., and Nie, M.: Differences in the temperature dependence of wetland CO<sub>2</sub> and CH<sub>4</sub>  
443 emissions vary with water table depth, *Nat. Clim. Chang.*, 11, 766–771, <https://doi.org/10.1038/s41558-021-01108-4>,  
444 2021.

445 Choulga, M., Janssens-Maenhout, G., Super, I., Solazzo, E., Agusti-Panareda, A., Balsamo, G., Bousserez, N., Crippa,  
446 M., Denier van der Gon, H., Engelen, R., Guizzardi, D., Kuenen, J., McNorton, J., Oreggioni, G., and Visschedijk, A.:  
447 Global anthropogenic CO<sub>2</sub> emissions and uncertainties as a prior for Earth system modelling and data assimilation, *Earth*  
448 *System Science Data*, 13, 5311–5335, <https://doi.org/10.5194/essd-13-5311-2021>, 2021.

449 Cintra, R. J. and Bayer, F. M.: A DCT Approximation for Image Compression, *IEEE Signal Processing Letters*, 18, 579–  
450 582, <https://doi.org/10.1109/LSP.2011.2163394>, 2011.

451 Crisp, D., Pollock, H. R., Rosenberg, R., Chapsky, L., Lee, R. A. M., Oyafuso, F. A., Frankenberg, C., O’Dell, C. W.,  
452 Bruegge, C. J., Doran, G. B., Eldering, A., Fisher, B. M., Fu, D., Gunson, M. R., Mandrake, L., Osterman, G. B.,  
453 Schwandner, F. M., Sun, K., Taylor, T. E., Wennberg, P. O., and Wunch, D.: The on-orbit performance of the Orbiting  
454 Carbon Observatory-2 (OCO-2) instrument and its radiometrically calibrated products, *Atmospheric Measurement*  
455 *Techniques*, 10, 59–81, <https://doi.org/10.5194/amt-10-59-2017>, 2017.

456 Crosswell, J. R., Anderson, I. C., Stanhope, J. W., Van Dam, B., Brush, M. J., Ensign, S., Piehler, M. F., McKee, B., Bost,  
457 M., and Paerl, H. W.: Carbon budget of a shallow, lagoonal estuary: Transformations and source-sink dynamics along  
458 the river-estuary-ocean continuum, *Limnology and Oceanography*, 62, S29–S45, <https://doi.org/10.1002/lno.10631>,  
459 2017.

460 Deng, F., Jones, D. B. A., Henze, D. K., Bousserez, N., Bowman, K. W., Fisher, J. B., Nassar, R., O’Dell, C., Wunch, D.,  
461 Wennberg, P. O., Kort, E. A., Wofsy, S. C., Blumenstock, T., Deutscher, N. M., Griffith, D. W. T., Hase, F., Heikkinen,  
462 P., Sherlock, V., Strong, K., Sussmann, R., and Warneke, T.: Inferring regional sources and sinks of atmospheric CO<sub>2</sub>  
463 from GOSAT XCO<sub>2</sub> data, *Atmospheric Chemistry and Physics*, 14, 3703–3727, [https://doi.org/10.5194/acp-14-3703-](https://doi.org/10.5194/acp-14-3703-464)  
464 2014, 2014.

465 Doughty, R., Kurosu, T. P., Parazoo, N., Köhler, P., Wang, Y., Sun, Y., and Frankenberg, C.: Global GOSAT, OCO-2, and  
466 OCO-3 solar-induced chlorophyll fluorescence datasets, *Earth System Science Data*, 14, 1513–1529,  
467 <https://doi.org/10.5194/essd-14-1513-2022>, 2022.

468 El-Mahallawy, M. S. and Hashim, M.: Material Classification of Underground Utilities From GPR Images Using DCT-  
469 Based SVM Approach, *IEEE Geoscience and Remote Sensing Letters*, 10, 1542–1546,  
470 <https://doi.org/10.1109/LGRS.2013.2261796>, 2013.

471 Fraser, A., Palmer, P. I., Feng, L., Boesch, H., Cogan, A., Parker, R., Dlugokencky, E. J., Fraser, P. J., Krummel, P. B.,  
472 Langenfelds, R. L., O’Doherty, S., Prinn, R. G., Steele, L. P., van der Schoot, M., and Weiss, R. F.: Estimating regional  
473 methane surface fluxes: the relative importance of surface and GOSAT mole fraction measurements, *Atmospheric*

- 474 Chemistry and Physics, 13, 5697–5713, <https://doi.org/10.5194/acp-13-5697-2013>, 2013.
- 475 Fredj, E., Roarty, H., Kohut, J., Smith, M., and Glenn, S.: Gap Filling of the Coastal Ocean Surface Currents from HFR  
476 Data: Application to the Mid-Atlantic Bight HFR Network, *Journal of Atmospheric and Oceanic Technology*, 33, 1097–  
477 1111, <https://doi.org/10.1175/JTECH-D-15-0056.1>, 2016.
- 478 Garcia, D.: Robust smoothing of gridded data in one and higher dimensions with missing values, *Computational*  
479 *Statistics & Data Analysis*, 54, 1167–1178, <https://doi.org/10.1016/j.csda.2009.09.020>, 2010.
- 480 Hakkarainen, J., Ialongo, I., and Tamminen, J.: Direct space-based observations of anthropogenic CO<sub>2</sub> emission areas  
481 from OCO-2, *Geophysical Research Letters*, 43, 11,400–11,406, <https://doi.org/10.1002/2016GL070885>, 2016.
- 482 Hamazaki, T., Kaneko, Y., Kuze, A., and Kondo, K.: Fourier transform spectrometer for Greenhouse Gases Observing  
483 Satellite (GOSAT), in: *Enabling Sensor and Platform Technologies for Spaceborne Remote Sensing*, *Enabling Sensor*  
484 *and Platform Technologies for Spaceborne Remote Sensing*, 73–80, <https://doi.org/10.1117/12.581198>, 2005.
- 485 He, C., Ji, M., Grieneisen, M. L., and Zhan, Y.: A review of datasets and methods for deriving spatiotemporal distributions  
486 of atmospheric CO<sub>2</sub>, *Journal of Environmental Management*, 322, 116101,  
487 <https://doi.org/10.1016/j.jenvman.2022.116101>, 2022a.
- 488 He, C., Ji, M., Li, T., Liu, X., Tang, D., Zhang, S., Luo, Y., Grieneisen, M. L., Zhou, Z., and Zhan, Y.: Deriving Full-  
489 Coverage and Fine-Scale XCO<sub>2</sub> Across China Based on OCO-2 Satellite Retrievals and CarbonTracker Output,  
490 *Geophysical Research Letters*, 49, e2022GL098435, <https://doi.org/10.1029/2022GL098435>, 2022b.
- 491 He, J., Yuan, Q., Li, J., and Zhang, L.: PoNet: A universal physical optimization-based spectral super-resolution network  
492 for arbitrary multispectral images, *Information Fusion*, 80, 205–225, <https://doi.org/10.1016/j.inffus.2021.10.016>, 2022c.
- 493 He, J., Yuan, Q., Li, J., Xiao, Y., Liu, D., Shen, H., and Zhang, L.: Spectral super-resolution meets deep learning:  
494 achievements and challenges, *Information Fusion*, 97, 101812, <https://doi.org/10.1016/j.inffus.2023.101812>, 2023.
- 495 He, Z., Lei, L., Zhang, Y., Sheng, M., Wu, C., Li, L., Zeng, Z.-C., and Welp, L. R.: Spatio-Temporal Mapping of Multi-  
496 Satellite Observed Column Atmospheric CO<sub>2</sub> Using Precision-Weighted Kriging Method, *Remote Sensing*, 12, 576,  
497 <https://doi.org/10.3390/rs12030576>, 2020.
- 498 Hong, X., Zhang, P., Bi, Y., Liu, C., Sun, Y., Wang, W., Chen, Z., Yin, H., Zhang, C., Tian, Y., and Liu, J.: Retrieval of  
499 Global Carbon Dioxide From TanSat Satellite and Comprehensive Validation With TCCON Measurements and Satellite  
500 Observations, *IEEE Transactions on Geoscience and Remote Sensing*, 60, 1–16,  
501 <https://doi.org/10.1109/TGRS.2021.3066623>, 2022.
- 502 Hotchkiss, E. R., Hall Jr, R. O., Sponseller, R. A., Butman, D., Klaminder, J., Laudon, H., Rosvall, M., and Karlsson, J.:  
503 Sources of and processes controlling CO<sub>2</sub> emissions change with the size of streams and rivers, *Nature Geosci*, 8, 696–  
504 699, <https://doi.org/10.1038/ngeo2507>, 2015.
- 505 Houweling, S., Baker, D., Basu, S., Boesch, H., Butz, A., Chevallier, F., Deng, F., Dlugokencky, E. J., Feng, L., Ganshin,  
506 A., Hasekamp, O., Jones, D., Maksyutov, S., Marshall, J., Oda, T., O'Dell, C. W., Oshchepkov, S., Palmer, P. I., Peylin,  
507 P., Poussi, Z., Reum, F., Takagi, H., Yoshida, Y., and Zhuravlev, R.: An intercomparison of inverse models for estimating  
508 sources and sinks of CO<sub>2</sub> using GOSAT measurements, *Journal of Geophysical Research: Atmospheres*, 120, 5253–5266,  
509 <https://doi.org/10.1002/2014JD022962>, 2015.
- 510 Jiang, F., Ju, W., He, W., Wu, M., Wang, H., Wang, J., Jia, M., Feng, S., Zhang, L., and Chen, J. M.: A 10-year global

511 monthly averaged terrestrial net ecosystem exchange dataset inferred from the ACOS GOSAT v9 XCO<sub>2</sub> retrievals  
512 (GCAS2021), *Earth System Science Data*, 14, 3013–3037, <https://doi.org/10.5194/essd-14-3013-2022>, 2022.

513 Katzfuss, M. and Cressie, N.: Tutorial on fixed rank kriging (FRK) of CO<sub>2</sub> data, Department of Statistics, The Ohio State  
514 University, Columbus, 2011.

515 Kenea, S. T., Lee, H., Patra, P. K., Li, S., Labzovskii, L. D., and Joo, S.: Long-term changes in CH<sub>4</sub> emissions: Comparing  
516  $\Delta\text{CH}_4/\Delta\text{CO}_2$  ratios between observation and proved model in East Asia (2010–2020), *Atmospheric Environment*, 293,  
517 119437, <https://doi.org/10.1016/j.atmosenv.2022.119437>, 2023.

518 Kiel, M., O'Dell, C. W., Fisher, B., Eldering, A., Nassar, R., MacDonald, C. G., and Wennberg, P. O.: How bias correction  
519 goes wrong: measurement of XCO<sub>2</sub> affected by erroneous surface pressure estimates, *Atmospheric Measurement*  
520 *Techniques*, 12, 2241–2259, <https://doi.org/10.5194/amt-12-2241-2019>, 2019.

521 Laughner, J. L., Roche, S., Kiel, M., Toon, G. C., Wunch, D., Baier, B. C., Biraud, S., Chen, H., Kivi, R., Laemmle, T.,  
522 McKain, K., Quéhé, P.-Y., Rousogonous, C., Stephens, B. B., Walker, K., and Wennberg, P. O.: A new algorithm to  
523 generate a priori trace gas profiles for the GGG2020 retrieval algorithm, *Atmospheric Measurement Techniques*  
524 *Discussions*, 1–41, <https://doi.org/10.5194/amt-2022-267>, 2022.

525 Le Quéré, C., Korsbakken, J. I., Wilson, C., Tosun, J., Andrew, R., Andres, R. J., Canadell, J. G., Jordan, A., Peters, G.  
526 P., and van Vuuren, D. P.: Drivers of declining CO<sub>2</sub> emissions in 18 developed economies, *Nat. Clim. Chang.*, 9, 213–  
527 217, <https://doi.org/10.1038/s41558-019-0419-7>, 2019.

528 Li, L., Lei, L., Song, H., Zeng, Z., and He, Z.: Spatiotemporal Geostatistical Analysis and Global Mapping of CH<sub>4</sub>  
529 Columns from GOSAT Observations, *Remote Sensing*, 14, 654, <https://doi.org/10.3390/rs14030654>, 2022.

530 Lin, X., Zhang, W., Crippa, M., Peng, S., Han, P., Zeng, N., Yu, L., and Wang, G.: A comparative study of anthropogenic  
531 CH<sub>4</sub> emissions over China based on the ensembles of bottom-up inventories, *Earth System Science Data*, 13, 1073–1088,  
532 <https://doi.org/10.5194/essd-13-1073-2021>, 2021.

533 Liu, J., Fung, I., Kalnay, E., and Kang, J.-S.: CO<sub>2</sub> transport uncertainties from the uncertainties in meteorological fields,  
534 *Geophysical Research Letters*, 38, <https://doi.org/10.1029/2011GL047213>, 2011.

535 Liu, L. and Greaver, T. L.: A review of nitrogen enrichment effects on three biogenic GHGs: the CO<sub>2</sub> sink may be largely  
536 offset by stimulated N<sub>2</sub>O and CH<sub>4</sub> emission, *Ecology Letters*, 12, 1103–1117, [https://doi.org/10.1111/j.1461-](https://doi.org/10.1111/j.1461-537)  
537 0248.2009.01351.x, 2009.

538 Liu, Y., Wang, J., Yao, L., Chen, X., Cai, Z., Yang, D., Yin, Z., Gu, S., Tian, L., Lu, N., and Lyu, D.: The TanSat mission:  
539 preliminary global observations, *Science Bulletin*, 63, 1200–1207, <https://doi.org/10.1016/j.scib.2018.08.004>, 2018.

540 Liu, Z., Liu, Z., Song, T., Gao, W., Wang, Y., Wang, L., Hu, B., Xin, J., and Wang, Y.: Long-term variation in CO<sub>2</sub>  
541 emissions with implications for the interannual trend in PM<sub>2.5</sub> over the last decade in Beijing, China, *Environmental*  
542 *Pollution*, 266, 115014, <https://doi.org/10.1016/j.envpol.2020.115014>, 2020.

543 Meinshausen, M., Meinshausen, N., Hare, W., Raper, S. C. B., Frieler, K., Knutti, R., Frame, D. J., and Allen, M. R.:  
544 Greenhouse-gas emission targets for limiting global warming to 2 °C, *Nature*, 458, 1158–1162,  
545 <https://doi.org/10.1038/nature08017>, 2009.

546 Montzka, S. A., Dlugokencky, E. J., and Butler, J. H.: Non-CO<sub>2</sub> greenhouse gases and climate change, *Nature*, 476, 43–  
547 50, <https://doi.org/10.1038/nature10322>, 2011.

548 Moran, D., Pichler, P.-P., Zheng, H., Muri, H., Klenner, J., Kramel, D., Többen, J., Weisz, H., Wiedmann, T., Wyckmans,  
549 A., Strømman, A. H., and Gurney, K. R.: Estimating CO<sub>2</sub> emissions for 10000 European cities, *Earth System Science*  
550 *Data*, 14, 845–864, <https://doi.org/10.5194/essd-14-845-2022>, 2022.

551 Mueller, T. G., Pusuluri, N. B., Mathias, K. K., Cornelius, P. L., Barnhisel, R. I., and Shearer, S. A.: Map quality for  
552 ordinary kriging and inverse distance weighted interpolation, *Soil Science Society of America Journal*, 68, 2042–2047,  
553 2004.

554 Parker, R. J., Webb, A., Boesch, H., Somkuti, P., Barrio Guillo, R., Di Noia, A., Kalaitzi, N., Anand, J. S., Bergamaschi,  
555 P., Chevallier, F., Palmer, P. I., Feng, L., Deutscher, N. M., Feist, D. G., Griffith, D. W. T., Hase, F., Kivi, R., Morino, I.,  
556 Notholt, J., Oh, Y.-S., Ohyama, H., Petri, C., Pollard, D. F., Roehl, C., Sha, M. K., Shiomi, K., Strong, K., Susmann, R.,  
557 Té, Y., Velazco, V. A., Warneke, T., Wennberg, P. O., and Wunch, D.: A decade of GOSAT Proxy satellite CH<sub>4</sub>  
558 observations, *Earth System Science Data*, 12, 3383–3412, <https://doi.org/10.5194/essd-12-3383-2020>, 2020.

559 Petrescu, A. M. R., Qiu, C., Ciais, P., Thompson, R. L., Peylin, P., McGrath, M. J., Solazzo, E., Janssens-Maenhout, G.,  
560 Tubiello, F. N., Bergamaschi, P., Brunner, D., Peters, G. P., Höglund-Isaksson, L., Regnier, P., Lauerwald, R., Bastviken,  
561 D., Tsuruta, A., Winiwarter, W., Patra, P. K., Kuhnert, M., Oreggioni, G. D., Crippa, M., Saunio, M., Perugini, L.,  
562 Markkanen, T., Aalto, T., Groot Zwaaftink, C. D., Tian, H., Yao, Y., Wilson, C., Conchedda, G., Günther, D., Leip, A.,  
563 Smith, P., Haussaire, J.-M., Leppänen, A., Manning, A. J., McNorton, J., Brockmann, P., and Dolman, A. J.: The  
564 consolidated European synthesis of CH<sub>4</sub> and N<sub>2</sub>O emissions for the European Union and United Kingdom: 1990–2017,  
565 *Earth System Science Data*, 13, 2307–2362, <https://doi.org/10.5194/essd-13-2307-2021>, 2021.

566 Pham, H. T., Kim, S., Marshall, L., and Johnson, F.: Using 3D robust smoothing to fill land surface temperature gaps at  
567 the continental scale, *International Journal of Applied Earth Observation and Geoinformation*, 82, 101879,  
568 <https://doi.org/10.1016/j.jag.2019.05.012>, 2019.

569 Rao, K. R. and Yip, P.: *Discrete Cosine Transform: Algorithms, Advantages, Applications*, Academic Press, 517 pp.,  
570 2014.

571 Reithmaier, G. M. S., Chen, X., Santos, I. R., Drexler, M. J., Holloway, C., Call, M., Álvarez, P. G., Euler, S., and Maher,  
572 D. T.: Rainfall drives rapid shifts in carbon and nutrient source-sink dynamics of an urbanised, mangrove-fringed estuary,  
573 *Estuarine, Coastal and Shelf Science*, 249, 107064, <https://doi.org/10.1016/j.ecss.2020.107064>, 2021.

574 Shine, K. P., Fuglestedt, J. S., Hailemariam, K., and Stuber, N.: Alternatives to the Global Warming Potential for  
575 Comparing Climate Impacts of Emissions of Greenhouse Gases, *Climatic Change*, 68, 281–302,  
576 <https://doi.org/10.1007/s10584-005-1146-9>, 2005.

577 Siabi, Z., Falahatkar, S., and Alavi, S. J.: Spatial distribution of XCO<sub>2</sub> using OCO-2 data in growing seasons, *Journal of*  
578 *Environmental Management*, 244, 110–118, <https://doi.org/10.1016/j.jenvman.2019.05.049>, 2019.

579 Sjögersten, S., Black, C. R., Evers, S., Hoyos-Santillan, J., Wright, E. L., and Turner, B. L.: Tropical wetlands: A missing  
580 link in the global carbon cycle?, *Global Biogeochemical Cycles*, 28, 1371–1386, <https://doi.org/10.1002/2014GB004844>,  
581 2014.

582 Solomon, S., Daniel, J. S., Sanford, T. J., Murphy, D. M., Plattner, G.-K., Knutti, R., and Friedlingstein, P.: Persistence  
583 of climate changes due to a range of greenhouse gases, *Proceedings of the National Academy of Sciences*, 107, 18354–  
584 18359, <https://doi.org/10.1073/pnas.1006282107>, 2010.

585 Taylor, T. E., O’Dell, C. W., Frankenberg, C., Partain, P. T., Cronk, H. Q., Savtchenko, A., Nelson, R. R., Rosenthal, E.  
586 J., Chang, A. Y., Fisher, B., Osterman, G. B., Pollock, R. H., Crisp, D., Eldering, A., and Gunson, M. R.: Orbiting Carbon

- 587 Observatory-2 (OCO-2) cloud screening algorithms: validation against collocated MODIS and CALIOP data,  
588 Atmospheric Measurement Techniques, 9, 973–989, <https://doi.org/10.5194/amt-9-973-2016>, 2016.
- 589 Taylor, T. E., O'Dell, C. W., Crisp, D., Kuze, A., Lindqvist, H., Wennberg, P. O., Chatterjee, A., Gunson, M., Eldering,  
590 A., Fisher, B., Kiel, M., Nelson, R. R., Merrelli, A., Osterman, G., Chevallier, F., Palmer, P. I., Feng, L., Deutscher, N.  
591 M., Dubey, M. K., Feist, D. G., García, O. E., Griffith, D. W. T., Hase, F., Iraci, L. T., Kivi, R., Liu, C., De Mazière, M.,  
592 Morino, I., Notholt, J., Oh, Y.-S., Ohyama, H., Pollard, D. F., Rettinger, M., Schneider, M., Roehl, C. M., Sha, M. K.,  
593 Shiomi, K., Strong, K., Sussmann, R., Té, Y., Velazco, V. A., Vrekoussis, M., Warneke, T., and Wunch, D.: An 11-year  
594 record of XCO<sub>2</sub> estimates derived from GOSAT measurements using the NASA ACOS version 9 retrieval algorithm,  
595 Earth System Science Data, 14, 325–360, <https://doi.org/10.5194/essd-14-325-2022>, 2022.
- 596 Turner, A. J., Jacob, D. J., Wecht, K. J., Maasakkers, J. D., Lundgren, E., Andrews, A. E., Biraud, S. C., Boesch, H.,  
597 Bowman, K. W., Deutscher, N. M., Dubey, M. K., Griffith, D. W. T., Hase, F., Kuze, A., Notholt, J., Ohyama, H., Parker,  
598 R., Payne, V. H., Sussmann, R., Sweeney, C., Velazco, V. A., Warneke, T., Wennberg, P. O., and Wunch, D.: Estimating  
599 global and North American methane emissions with high spatial resolution using GOSAT satellite data, Atmospheric  
600 Chemistry and Physics, 15, 7049–7069, <https://doi.org/10.5194/acp-15-7049-2015>, 2015.
- 601 Velazco, V. A., Deutscher, N. M., Morino, I., Uchino, O., Bukosa, B., Ajiro, M., Kamei, A., Jones, N. B., Paton-Walsh,  
602 C., and Griffith, D. W. T.: Satellite and ground-based measurements of XCO<sub>2</sub> in a remote semiarid region of Australia,  
603 Earth System Science Data, 11, 935–946, <https://doi.org/10.5194/essd-11-935-2019>, 2019.
- 604 Wang, G., Garcia, D., Liu, Y., de Jeu, R., and Johannes Dolman, A.: A three-dimensional gap filling method for large  
605 geophysical datasets: Application to global satellite soil moisture observations, Environmental Modelling & Software,  
606 30, 139–142, <https://doi.org/10.1016/j.envsoft.2011.10.015>, 2012.
- 607 Wang, H., Jiang, F., Wang, J., Ju, W., and Chen, J. M.: Terrestrial ecosystem carbon flux estimated using GOSAT and  
608 OCO-2 XCO<sub>2</sub> retrievals, Atmospheric Chemistry and Physics, 19, 12067–12082, [https://doi.org/10.5194/acp-19-12067-](https://doi.org/10.5194/acp-19-12067-2019)  
609 2019, 2019.
- 610 Wang, T., Yu, P., Wu, Z., Lu, W., Liu, X., Li, Q. P., and Huang, B.: Revisiting the Intraseasonal Variability of Chlorophyll-  
611 a in the Adjacent Luzon Strait With a New Gap-Filled Remote Sensing Data Set, IEEE Transactions on Geoscience and  
612 Remote Sensing, 60, 1–11, <https://doi.org/10.1109/TGRS.2021.3067646>, 2022a.
- 613 Wang, Y., Yuan, Q., Li, T., Zhu, L., and Zhang, L.: Estimating daily full-coverage near surface O<sub>3</sub>, CO, and NO<sub>2</sub>  
614 concentrations at a high spatial resolution over China based on S5P-TROPOMI and GEOS-FP, ISPRS Journal of  
615 Photogrammetry and Remote Sensing, 175, 311–325, 2021.
- 616 Wang, Y., Yuan, Q., Li, T., and Zhang, L.: Global long-term (2010-2020) daily seamless fused XCO<sub>2</sub> and XCH<sub>4</sub> from  
617 CAMS, OCO-2, and GOSAT, <https://doi.org/10.5281/zenodo.7388893>, 2022b.
- 618 Wang, Y., Yuan, Q., Li, T., and Zhu, L.: Global spatiotemporal estimation of daily high-resolution surface carbon  
619 monoxide concentrations using Deep Forest, Journal of Cleaner Production, 350, 131500, 2022c.
- 620 Wu, L., Hasekamp, O., Hu, H., Landgraf, J., Butz, A., aan de Brugh, J., Aben, I., Pollard, D. F., Griffith, D. W. T., Feist,  
621 D. G., Koshelev, D., Hase, F., Toon, G. C., Ohyama, H., Morino, I., Notholt, J., Shiomi, K., Iraci, L., Schneider, M., de  
622 Mazière, M., Sussmann, R., Kivi, R., Warneke, T., Goo, T.-Y., and Té, Y.: Carbon dioxide retrieval from OCO-2 satellite  
623 observations using the RemoTeC algorithm and validation with TCCON measurements, Atmospheric Measurement  
624 Techniques, 11, 3111–3130, <https://doi.org/10.5194/amt-11-3111-2018>, 2018.
- 625 Wunch, D., Toon, G. C., Blavier, J.-F. L., Washenfelder, R. A., Notholt, J., Connor, B. J., Griffith, D. W. T., Sherlock, V.,

- 626 and Wennberg, P. O.: The Total Carbon Column Observing Network, *Philosophical Transactions of the Royal Society A:*  
627 *Mathematical, Physical and Engineering Sciences*, 369, 2087–2112, <https://doi.org/10.1098/rsta.2010.0240>, 2011.
- 628 Wunch, D., Wennberg, P. O., Osterman, G., Fisher, B., Naylor, B., Roehl, C. M., O'Dell, C., Mandrake, L., Viatte, C.,  
629 Kiel, M., Griffith, D. W. T., Deutscher, N. M., Velasco, V. A., Notholt, J., Warneke, T., Petri, C., De Maziere, M., Sha,  
630 M. K., Sussmann, R., Rettinger, M., Pollard, D., Robinson, J., Morino, I., Uchino, O., Hase, F., Blumenstock, T., Feist,  
631 D. G., Arnold, S. G., Strong, K., Mendonca, J., Kivi, R., Heikkinen, P., Iraci, L., Podolske, J., Hillyard, P. W., Kawakami,  
632 S., Dubey, M. K., Parker, H. A., Sepulveda, E., García, O. E., Te, Y., Jeseck, P., Gunson, M. R., Crisp, D., and Eldering,  
633 A.: Comparisons of the Orbiting Carbon Observatory-2 (OCO-2) XCO<sub>2</sub> measurements with TCCON, *Atmospheric*  
634 *Measurement Techniques*, 10, 2209–2238, <https://doi.org/10.5194/amt-10-2209-2017>, 2017.
- 635 Xiao, Y., Yuan, Q., He, J., Zhang, Q., Sun, J., Su, X., Wu, J., and Zhang, L.: Space-time super-resolution for satellite  
636 video: A joint framework based on multi-scale spatial-temporal transformer, *International Journal of Applied Earth*  
637 *Observation and Geoinformation*, 108, 102731, <https://doi.org/10.1016/j.jag.2022.102731>, 2022.
- 638 Xiao, Y., Yuan, Q., Jiang, K., He, J., Wang, Y., and Zhang, L.: From degrade to upgrade: Learning a self-supervised  
639 degradation guided adaptive network for blind remote sensing image super-resolution, *Information Fusion*, 96, 297-311,  
640 <https://doi.org/10.1016/j.inffus.2023.03.021>, 2023.
- 641 Yoro, K. O. and Daramola, M. O.: Chapter 1 - CO<sub>2</sub> emission sources, greenhouse gases, and the global warming effect,  
642 in: *Advances in Carbon Capture*, edited by: Rahimpour, M. R., Farsi, M., and Makarem, M. A., Woodhead Publishing,  
643 3–28, <https://doi.org/10.1016/B978-0-12-819657-1.00001-3>, 2020.
- 644 Yoshida, Y., Kikuchi, N., Morino, I., Uchino, O., Oshchepkov, S., Bril, A., Saeki, T., Schutgens, N., Toon, G. C., Wunch,  
645 D., Roehl, C. M., Wennberg, P. O., Griffith, D. W. T., Deutscher, N. M., Warneke, T., Notholt, J., Robinson, J., Sherlock,  
646 V., Connor, B., Rettinger, M., Sussmann, R., Ahonen, P., Heikkinen, P., Kyrö, E., Mendonca, J., Strong, K., Hase, F.,  
647 Dohe, S., and Yokota, T.: Improvement of the retrieval algorithm for GOSAT SWIR XCO<sub>2</sub> and XCH<sub>4</sub> and their validation  
648 using TCCON data, *Atmospheric Measurement Techniques*, 6, 1533–1547, <https://doi.org/10.5194/amt-6-1533-2013>,  
649 2013.
- 650 Zhang, L., Li, T., and Wu, J.: Deriving gapless CO<sub>2</sub> concentrations using a geographically weighted neural network:  
651 China, 2014–2020, *International Journal of Applied Earth Observation and Geoinformation*, 114, 103063,  
652 <https://doi.org/10.1016/j.jag.2022.103063>, 2022.
- 653 Zhang, M. and Liu, G.: Mapping contiguous XCO<sub>2</sub> by machine learning and analyzing the spatio-temporal variation in  
654 China from 2003 to 2019, *Science of The Total Environment*, 858, 159588,  
655 <https://doi.org/10.1016/j.scitotenv.2022.159588>, 2023.
- 656 Zhou, S., Wang, Y., Yuan, Q., Yue, L., and Zhang, L.: Spatiotemporal estimation of 6-hour high-resolution precipitation  
657 across China based on Himawari-8 using a stacking ensemble machine learning model, *Journal of Hydrology*, 609,  
658 127718, 2022.

659